KTH Engineering Sciences

Studies of Neutron Backgrounds for PoGOLite – a Balloon-borne Gamma-ray Polarimeter

Jaroslav Kazejev

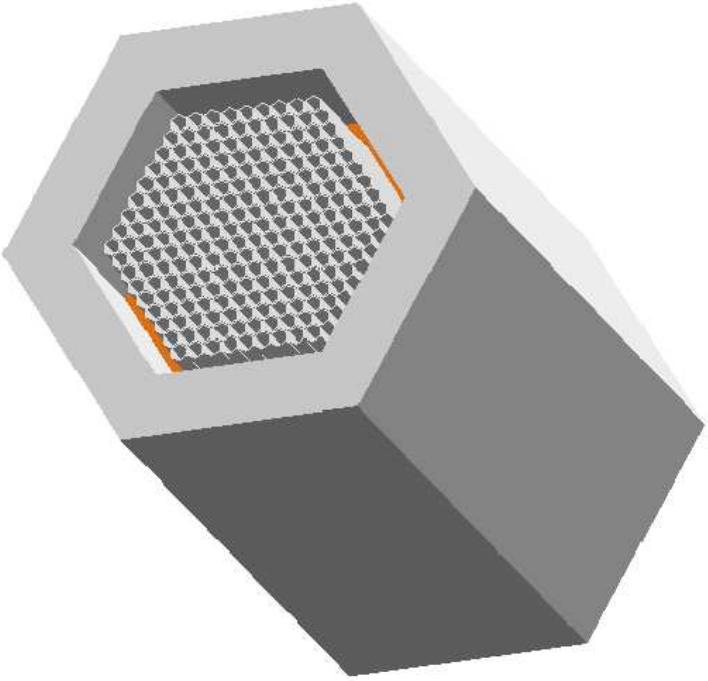

Master's thesis
KTH, 2007

Typeset in LaTeX

ISRN KTH/FYS/– –07:62– –SE
ISSN 0280-316X
TRITA-FYS-2007:62

Abstract

PoGOLite is a balloon-borne experiment that will measure polarisation of X-rays and gamma-rays in the energy range 25–80 keV for a 200 mCrab source. Polarised gamma-rays are expected from a variety of celestial sources including rotation powered pulsars, accreting black holes, neutrons stars and jets from active galaxies. To this day, polarisation has only been measured for the Crab nebula at 2.6 keV and 5.2 keV by the OSO-8 satellite in 1976.

In this thesis is presented a study, performed using Monte Carlo simulations in Geant4, of the atmospheric neutron background and its effect on the flux measured during observations. The neutron background is shown to be higher than expected and the anticoincidence system of PoGOLite is not effective against this background. As a result of this study a polyethylene passive neutron shield is introduced in the design. This shield is successful at blocking and moderating neutrons and as a result of this the neutron background is reduced to acceptable levels. The effectiveness of the anticoincidence system against neutrons increases when used together with the polyethylene shield. The effect of neutrons induced by protons in the aluminium gondola structure supporting PoGOLite is also examined. The background generated by this source is shown to be negligible.

Contents

Chapter 1

Introduction

1.1 Background

Polarised gamma-rays are expected from a variety of celestial sources including rotation powered pulsars, accreting black holes, neutrons stars and jets from active galaxies. To this day, polarisation has only been measured for the Crab nebula at 2.6 keV and 5.2 keV by the OSO-8 satellite in 1976 [1]. The Polarised Gamma-ray Observer - Lightweight version (PoGOLite) is a balloon-borne soft gamma-ray polarimeter that will provide a probe into high-energy emission mechanisms, the distribution of magnetic fields and interstellar matter. It is designed to measure polarisation in the energy range 25–80 keV for a 200 mCrab source. PoGOLite is planned to fly six hour long flights from Palestine in Texas and on long-duration flights from Sweden to Canada.

Gamma-rays are attenuated in the atmosphere, therefore the experiment will be launched to an altitude of ∼41–42 km, where gamma-rays above ∼25 keV can be observed. At this altitude the environment is rich on cosmic rays that can provide a background noise during observations. Neutrons are produced in the atmosphere by cosmic-ray protons. The results of this study show that the original belief that the background induced by neutrons would be no higher than that of gamma rays was wrong. A neutron shield is therefore introduced.

The rest of this chapter covers the scientific goals of the project and the design of the PoGOLite detector [2]. Chapter 2 gives a theoretical background on cosmic rays, the mechanisms by which neutrons interact in matter and some of the physics involved. In chapter 3 the implementation of PoGOLite and simulation procedures are described and in chapter 4 the results of this study are presented. The conclusions of this work are presented in chapter 5.

1.2 Scientific objectives of PoGOLite

1.2.1 Pulsars

The so-called *rotation-powered pulsars* are rapidly rotating neutron stars of which the Crab pulsar is a prime target for polarisation measurements with PoGOLite. Their X-ray and gamma-ray spectra show two peaks, P1 and P2 shown in figure 1.1. Three different models describe the emissions and a phase-resolved polarisation measurement will show where in the magnetosphere the emission occurs.

In the *polar cap* model [3, 4] particles are accelerated in a high magnetic field near the

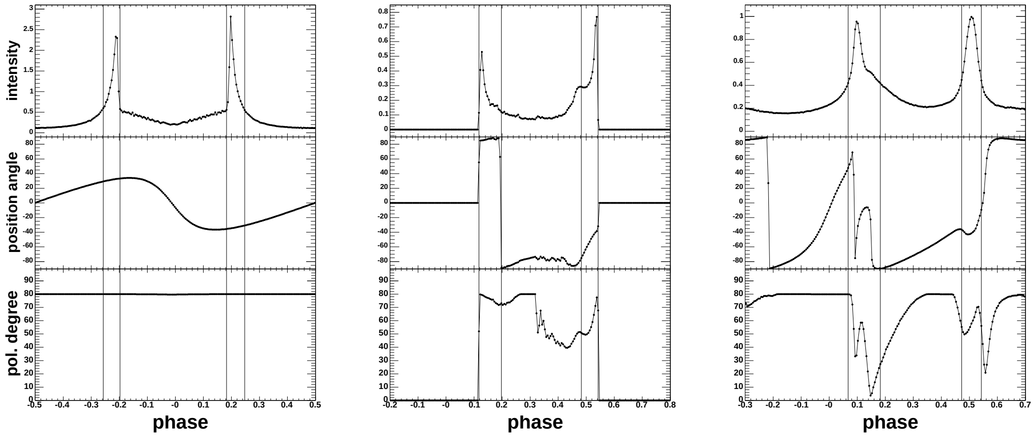

Figure 1.1: Model predictions for the three Crab pulsar modes [2]. Left: the polar cap model, center: the outer gap model, right: the caustic model. The top row shows intensity as relative flux, the middle row shows polarisation position angle in degrees and the bottom row shows polarisation degree in percent. The two pulses P1 and P2 are marked by a pair of vertical lines.

star surface and emission results from curvature radiation and inverse Compton-induced pair cascades. In *outer gap* models [5] acceleration occurs in the outer magnetosphere along the last open field line and emission results from photon-photon pair-production induced cascades. The polarisation produced by these mechanisms is highly polarised, up to 70%. In the *caustic* model the emission occurs at both poles whereas in the two other models emission is seen from only one region.

PoGOLite will distinguish between these models by using P1 alone. The measurements will also provide useful data for understanding the emission mechanism of pulsars.

1.2.2 Accreting black holes

Cygnus X-1 is a binary system in which a compact object, such as a black hole, accretes material from a companion star. The material in the fast rotating accretion disk that is formed reaches temperatures high enough to emit X-rays. Two major states can be seen in the emission spectrum that are related to the accretion rate. In the *hard state* a hot inner flow is formed on the accretion disk close to the black hole. the accretion rate is high and the accretion disk geometrically thin, optically thick and extending into the innermost stable orbit of the black hole. Thermal X-ray photons in the outer part of the disk are Compton up-scattered by electrons from the inner flow which results in a hard X-ray spectrum. Also, hard X-ray photons are reflected off the cooler accretion disk. This reflected component is expected to be highly polarised. The inclination of the system also affects the polarisation and can thus be derived from polarimetry measurements.

In the *soft state* energetic electrons in active regions above the accretion disk Compton up-scatter photons in the accretion disk. This state is expected to have a different polarisation signature than the hard state. Polarisation measurements will provide a test for the models and put constraints on the geometry of the accreting system.

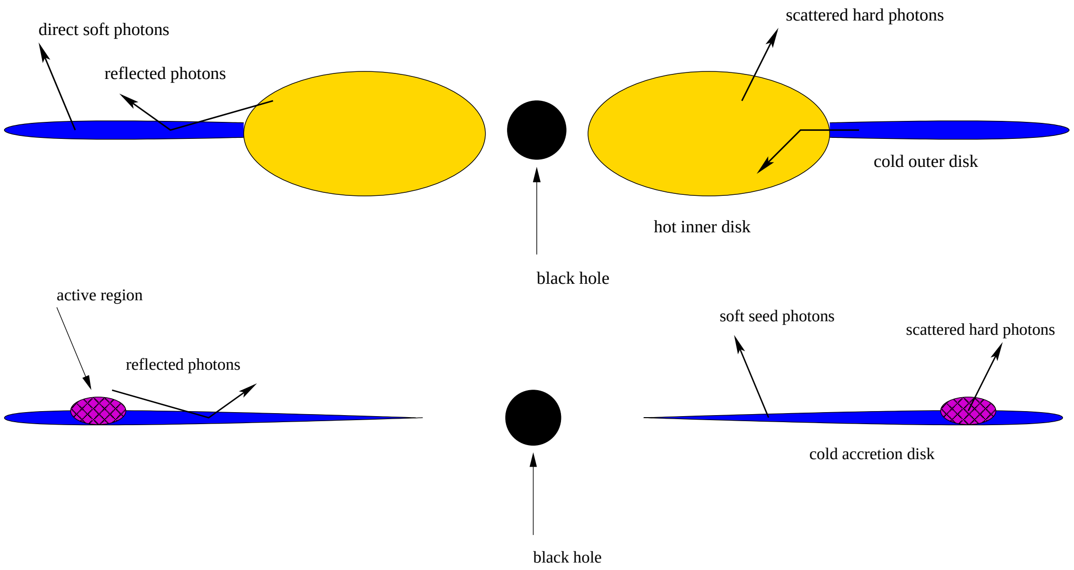

Figure 1.2: Schematic picture of the two states of Cygnus X-1. Top: hard state, bottom: soft state.

1.2.3 Accreting neutron stars

Neutron stars with a high magnetic field of order 10^{12} Gauss such as Hercules X-1 provides a unique opportunity to study physical processes under extreme conditions. Material accretes along magnetic field lines onto the polar regions. In the strong magnetic field, electrons will gyrate in a plane perpendicular to the magnetic field and interact more easily with photons whose electric field is perpendicular to the magnetic field. Scattering will depend on the polarisation angle which results in emitted X-rays having a probability to be polarised. Rotation of the neutron star modulates the direction and strength of the polarisation. Polarimetry will make it possible to determine the orientation of the rotation and the magnetic axis axis of the star.

There are two models describing the emission process. Either a stand-off shock is formed and the emission is normal to the magnetic field and comes from a vertical accretion column or hot plasma slabs are formed in deceleration by Coulomb collisions that result in emission in the vertical direction. These models predict opposite correlations between flux and polarization. Polarization measurements will distinguish between these two models.

1.3 Description of PoGOLite

1.3.1 Design

PoGOLite is an instrument designed measure polarisation by detecting the Compton scattering angle of incoming gamma-rays. An incoming photon from the observed source will presumably deposit energy at two or more locations in the detector, the first will be a Compton scattering site and at the final deposition it will be photo-absorbed. More than one Compton scattering may occur in a series of depositions. The detector consists of several units that each can register these energy depositions. The Compton scattering and photo absorption processes will be described later in chapter 2. In order to eliminate signals from

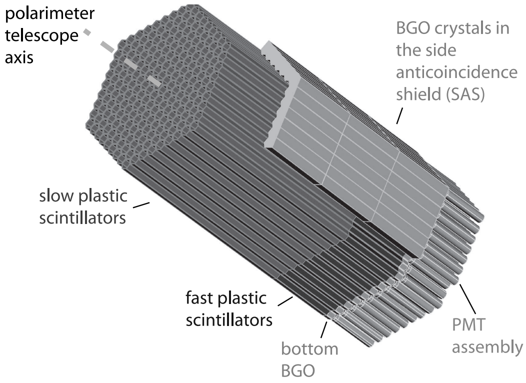

Figure 1.3: Overview drawing of the PoGOLite detector assembly. From [2].

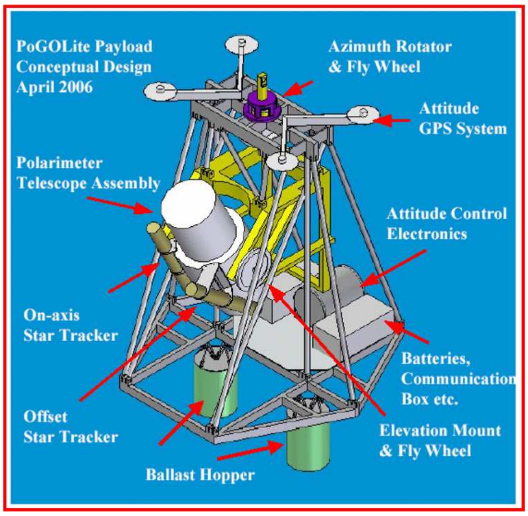

Figure 1.4: The gondola structure supporting PoGOLite. From [6].

background radiation and “unclean” signals (from photons that are scattered out), PoGOLite employs both active and passive shielding. A complete description of the design can be found in [2].

The PoGOLite detector assembly consists of 217 phoswich detector cells (PDCs) that are tightly packed in a hexagonal array and 54 side anti-coincidence detectors made of BGO (Bismuth germanate, $Bi_4Ge_3O_{12}$) scintillators. Figure 1.3 shows this arrangement. In order to reduce systematic errors in polarisation measurement this assembly is placed in a cylinder that rotates around its longitudinal axis. This is in turn placed in another cylindrical structure that is filled with polyethylene. The polyethylene acts as neutron shield or moderator and was introduced during the course of this study, the original design did not have this feature. A cut-through drawing of the final design of the detector assembly and the cylindrical structures is shown in figure 5.1. The balloon gondola structure that will support PoGOLite is shown in figure 1.4. The gondola design has been adopted from the flight-proven design of the High Energy Focusing Telescope (HEFT).

Each PDC consist of a 60 cm long slow plastic scintillator, a 20 cm long fast plastic scintillator and a 4 cm long BGO scintillator. At the BGO end of the PDC a photomultiplier is attached. Scintillators and photomultiplicators are described in sections 2.6 and 2.7. The slow plastic scintillator is hollow with thin walls and acts as an active collimator, it defines a solid angle for observations which is 1.25 msr ($2.0° \times 2.0°$). It is also wrapped by thin lead and tin foils that provides passive collimation. The fast scintillators are the main detectors.

The plastic scintillators are named according to their fluorescence decay time, which for the fast and slow scintillators is 285 ns and approximately 2 ns, respectively while BGO scintillators have a decay time of roughly 300 ns. The different time response characteristics makes it possible to determine from which of the scintillators in a PDC light is emitted by analysing the waveform of the output signal.

The *veto system*, which is designed to detect unwanted background radiation consists of the side anti-coincidence system, the bottom BGO scintillators of the PDCs and the slow plastic scintillators. In order for an event to be valid, there must not be a signal from the veto system. While the side shield consists of 54 rods in the actual design, it is simulated as

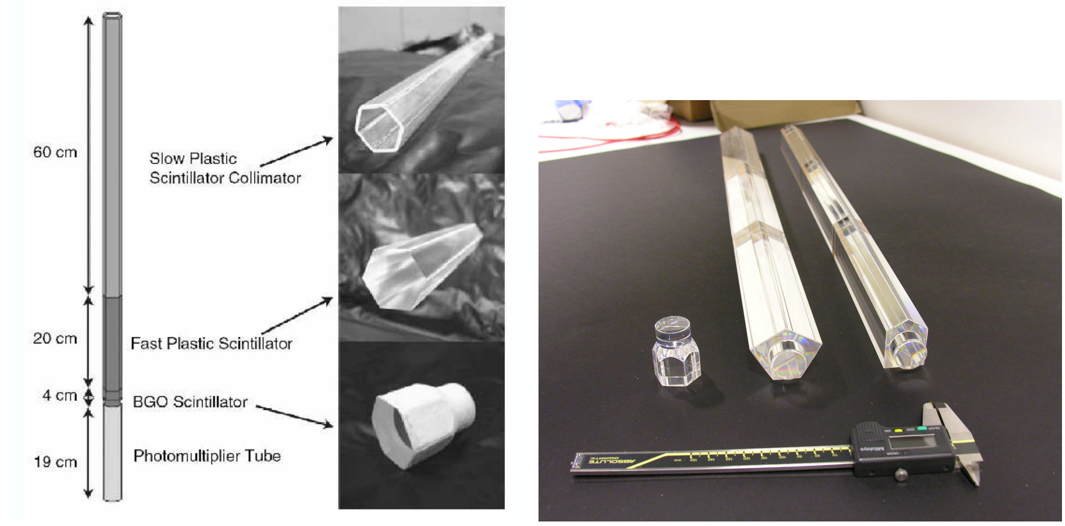

Figure 1.5: Left: The composition of a phoswich detector cell. From top a 60 cm long slow plastic scintillator well, a 20 cm fast plastic scintillator rod, a 4 cm long BGO crystal and a 19 cm long photomultiplier tube. Right: The three types of BGO crystals used for the anticoincidence system; a bottom BGO crystal, a corner edge and a side rod. From [2].

a single piece. This has the implication that the small gaps ($\sim$100 μm) between the rods are not taken into account in the simulations. The anti-coincidence threshold is 75 keV for the BGO and 30 keV for the slow plastic scintillators.

1.3.2 Data processing

Signals from all PMTs are digitised and processed by on-board logic. If a signal from a fast scintillator is detected and no veto signal is issued the wave forms of all PMTs are stored during a period of time for later analysis.

The off line analysis will be done in the following way. First select the PDC which recorded the photo-absorption. Assuming that photo-absorption leaves a higher energy deposit than a Compton scattering this will be the site with the highest energy deposit. Next, search neighboring sites, up to two layers, from the photo-absorption site for a Compton scattering signal. If more than one site is found the site with the highest signal is selected. Here is a difference to the simulated procedure, in which the Compton scattering site is allowed to be in any other PDC. The azimuthal angle of the scattering can now be determined as the line connecting the centers of the two PDCs.

Figure 1.6 shows reconstructed modulation curves of Compton scattering azimuthal angles predicted for P1 of the Crab pulsar for three pulsar models.

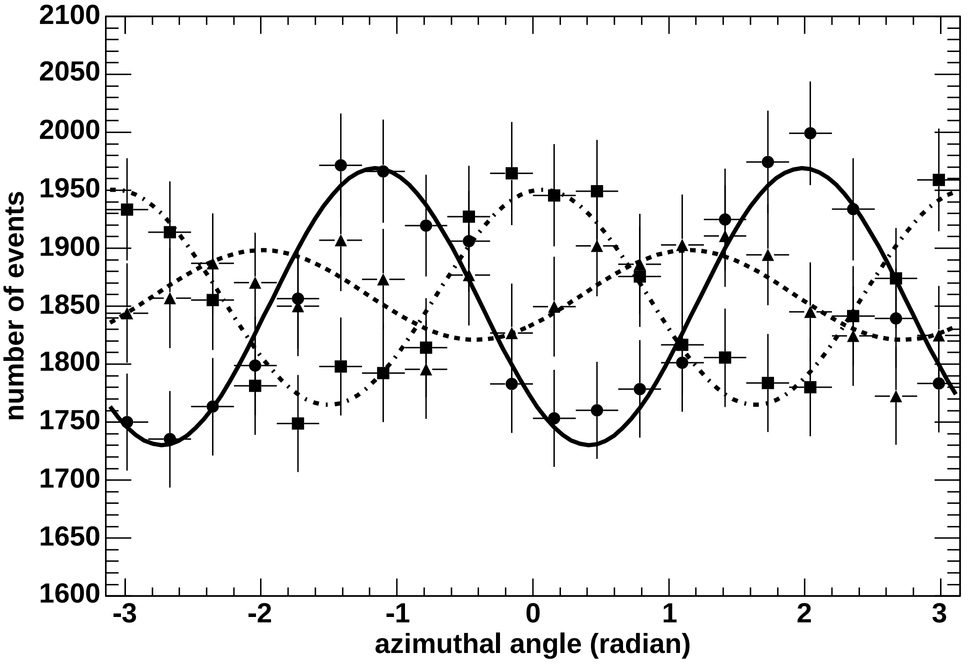

Figure 1.6: Modulation in the azimuthal Compton scattering angle predicted for P1 of the Crab pulsar by three pulsar models: (solid) polar cap model; (dashed) outer gap model; (dot-dashed) caustic model. A 6 hour simulated observation by PoGOLite at 4 g/cm^3 atmospheric overburden is shown. From [2].

Chapter 2

Theory

2.1 Introduction

This chapter introduces various topics that are of relevance to the function of PoGOLite and the neutron background. First, the main processes by which neutrons interact in matter are described. After that, cosmic rays that induce atmospheric neutrons are described. PoGOLite detects polarisation by utilising the Compton scattering effect, this effect is described together with other photon interactions in section 2.3 and after that comes a description of the scintillators and photomultipliers that are used in PoGOLite.

2.2 Neutron interactions in matter

The neutron lacks electric charge, so it is not affected by Coulomb interactions with the electrons and nuclei in matter. It interacts with nuclei through the strong force which has a shorter range. The fact that normal matter is mainly empty space therefore makes the neutron a very penetrating particle.

The processes by which neutrons may interact with the detector material are *neutron absorption* (n, γ) *inelastic scattering* (n, n$'$) and *elastic scattering*. Other interactions such as *nuclear reactions* and *fission* may occur but their contribution in the context of PoGOLite is negligible.

When a neutron collides with a target nucleus it can lose its kinetic energy in collisions with the target's constituent nucleons until it becomes an indistinguishable part of it. The energy state of the *compound nucleus* formed this way will have energy contributions from both the kinetic energy of the incoming neutron and from the binding energy released when it is absorbed into the target nucleus. If total center-of-mass energy, which is the sum of the kinetic energy of the neutron and its and the target nucleus rest mass energy, corresponds to an excited state in the compound nucleus, there is a large probability that it will be formed in that excited state.

2.2.1 Neutron absorption

Neutron absorption (n, γ) is a process in which a neutron is captured by a nucleus and the resulting composite nucleus is formed in an excited state with an energy level equal to its binding energy. This energy can be emitted as a gamma ray when de-excitation occurs. In plastic scintillators, deuterium can be formed when a neutron is captured by a hydrogen nucleus. Deuterium has a binding energy of 2.2 MeV which is emitted as a photon. The cross section of this process is generally high (order of 10^2 barns or higher) for thermal neutrons and decreases with the kinetic energy of the neutron v, as $1/v$.

2.2.2 Inelastic scattering

Inelastic scattering occurs when a nucleus is excited to a higher level energy state by a colliding neutron. A gamma ray photon is emitted upon de-excitation. The energy required for such excitation is [7]

$$E = \frac{(m_n + M)\epsilon}{M} \tag{2.1}$$

where m_n and M are the masses of the neutron and the target nucleus respectively and ϵ is the energy level of the state.

2.2.3 Elastic scattering

Elastic scattering is a collision after which the total kinetic energy is the same as the kinetic energy before. In this kind of interaction a portion of the neutron kinetic energy is transfered to a target nucleus, which recoils. If the *recoil nucleus* is light, it will behave much like a proton or alpha particle as it deposits energy in the target material.

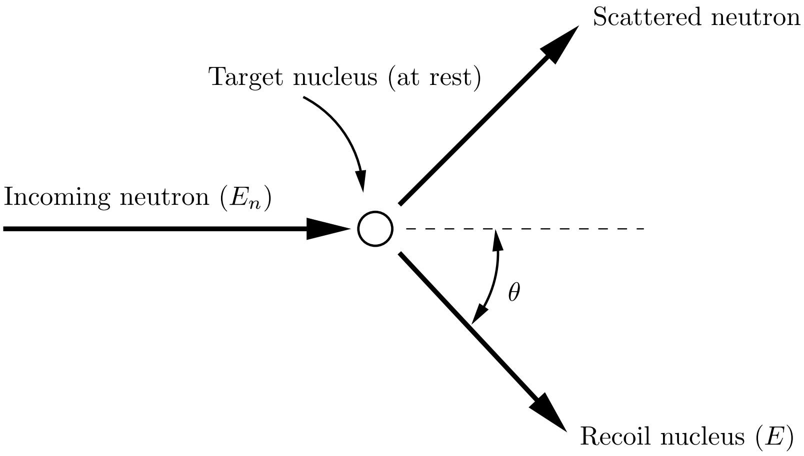

Figure 2.1: Elastic scattering of a neutron.

For neutrons with non-relativistic ($E_n << 939$ MeV) energy colliding with a target nucleus at rest, the energy transfered to the target nucleus can be described as [8]

$$E = \frac{4A}{(1 + A)^2}(\cos^2\theta)E_n \tag{2.2}$$

Here, A is the mass of target nucleus, E_n is the incoming neutron kinetic energy and θ is the scattering angle of the recoil nucleus, all in the laboratory coordinate system. It is seen here that the lighter the target nucleus, the larger is the portion of energy that can be transfered. The maximum possible energy transfer occurs for a head-on collision, then $\theta = 0$ and the recoil energy is

$$E = \frac{4A}{(1 + A)^2}E_n. \tag{2.3}$$

For hydrogen ($^1_1$H), with $A = 1$, the equation (2.3) gives $E/E_n = 1$. For a heavier nucleus, such as carbon ($^{12}_6$C), with $A = 12$, equation (2.3) gives $E/E_n \approx 0.284$. This shows that materials that has a high content of hydrogen, such as plastic or polyethylene, act as good neutron moderators.

2.3 Photon interactions

A photon can interact with matter by three main processes: *photoelectric effect, Compton scattering* and *pair production*. The principal qualitative feature of these processes is that photons are either scattered or completely absorbed.

2.3.1 Photoelectric effect

A photon may be absorbed by an atomic electron. If the transfered energy is greater than the binding energy of the electron, the electron is ejected with an energy

$$E = h\nu - \phi, \tag{2.4}$$

where $h = 4.13570 \cdot 10^{-15}$ eV·s is Planck's constants, ν is the frequency of the photon and ϕ is the binding energy. Conservation of momentum requires that the electron is bound to a nucleus that absorbs the recoil momentum, the photoelectric effect can not occur on free electrons.

2.3.2 Compton scattering

Compton scattering is the scattering of photons on free electrons. The photon interacts with an electron, transferring a part of its energy while scattering in a different direction. Electrons bound to atoms can be considered free if the photon energy is high compared to the binding energy. The scattering process is illustrated in figure 2.2 which shows a photon with energy E being scattered at an angle θ relative its incident direction. The energy of the

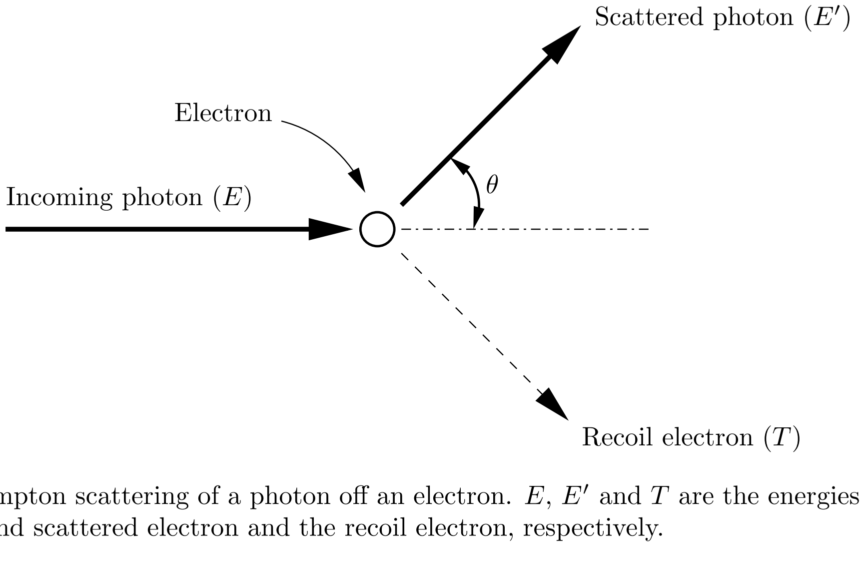

Figure 2.2: Compton scattering of a photon off an electron. E, E' and T are the energies of the incoming and scattered electron and the recoil electron, respectively.

scattered photon, E', is given by [9]

$$E' = \frac{E}{1+\gamma(1-\cos\theta)}, \tag{2.5}$$

where $\gamma = E/m_e c^2$ (m_e being the electron mass and c the speed of light). The electron is recoiled with a kinetic energy

$$T = E - E' = E\frac{\gamma(1-\cos\theta)}{1+\gamma(1-\cos\theta)}. \tag{2.6}$$

Scattering of photons can be described by the Klein-Nishina cross section of Compton scattering [10], which is given by

$$\frac{\mathrm{d}\sigma}{\mathrm{d}\Omega} = \frac{1}{2} r_0^2 \frac{k^2}{k_0^2}\left[\frac{k}{k_0} + \frac{k_0}{k} - 2\sin^2\theta\cos^2\phi\right]. \tag{2.7}$$

Here k and k_0 are the momentum vectors of the incident and scattered photon and r_0 is the classical electron radius $r_0 = e^2/(4\pi\epsilon_0 m_e c^2)$ (where e is the absolute value of the electron charge and ϵ_0 is the permittivity of free space). Figure 2.3, in which a completely polarised photon is scattered at point O, shows the geometry of this scattering. Assuming that the photon travels along the z-axis and the polarisation vector is along the x-axis, θ and ϕ will be the polar and azimuth angles of the scattering. This shows that scattering is more likely to occur in and close to directions at right angles ($\phi \in \{\pi/2, 3\pi/2\}$) to the direction of the incident polarisation vector and is less probable in directions along the incident polarisation vector ($\phi \in \{0, \pi\}$). When looking at a source of polarised photons the azimuth angles of the scatterings will be distributed according to $\cos^2\phi$. This is used to calculate the polarisation of the observed radiation.

2.3.3 Pair production

An electron may undergo *pair production* and transform to an electron-positron pair. In order to conserve momentum a third body must be present, usually a nucleus. The energy of the electron must be greater than the rest mass energy of the produced pair, i.e. $E \geq 2m_e c^2$, which is 1022 keV.

2.4 Cosmic ray background

Cosmic rays are particles that originate from various sources in space. Despite the name, cosmic rays consist of particles rather than continuous rays although there are sources of electromagnetic radiation in space that contribute to background. Most of the cosmic rays are hydrogen and helium nuclei, and electrons. The cosmic radiation environment at Earth consists of three main components: trapped radiation, galactic cosmic rays and solar particle events.

2.4.1 Solar wind

The solar wind is a plasma of ionized hydrogen and helium that flows out from the sun. This plasma carries magnetic field lines from the sun along with the wind which forms the *interplanetary magnetic field*, that together with the Sun's rotation forms a spiral.

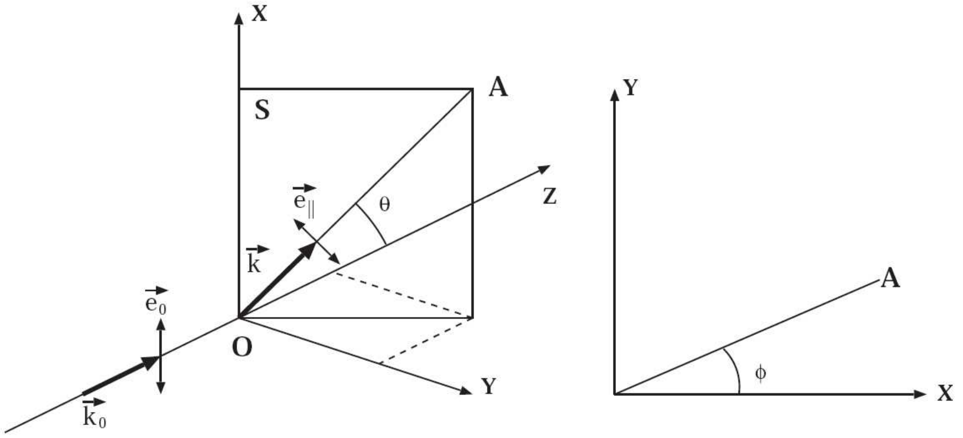

Figure 2.3: A completely linearly polarised photon is scattered at point O. The momentum vector $\vec{k_0}$ and the polarisation vector $\vec{e}_0$ are along the z- and x-axis, respectively, while $\vec{k}$ is the momentum vector after scattering. Plane S is constructed by $\vec{e}_0$ and $\vec{k}$ and contains $\vec{e}_{\|}$. The polar scattering angle is θ and the azimuth angle is ϕ. From [10].

The activity of the sun is cyclic, following a period of 22 years. The cycles originate from variations in the solar magnetic field which, from a well defined dipole, breaks down and reappears as a dipole with reversed polarity. The features of the sun are not dependent on polarity of the field and thus the sun exhibits a cycle of eleven years. The phase of the solar cycle can be determined by observation of *sunspots*, which are more frequent at *solar maximum* when the dipole field is broken down due to increased magnetic activity. The state with a well defined dipole field results in less magnetic activity and is referred to as *solar minimum.* The solar wind also follows the solar cycle and is stronger at solar maximum than at solar minimum. *Solar Particle Events* (SPEs) usually occur during solar maximum and result in protons being accelerated to hundreds of MeV. When PoGOLite will fly in 2010 the solar activity will be approaching a maximum [11].

2.4.2 Galactic cosmic rays

Galactic cosmic rays (GCRs) originate outside the solar system and consist of 90 % protons, 9 % alpha particles and 1 % heavier nuclei that span a wide energy range up to 10^{19} GeV/nucleon. The intensity of the GCR flux decreases with increasing energy. They are believed to be a result of acceleration of particles to near speed of light in supernova remnants. The GCR flux is modulated by the interplanetary magnetic field, leading to lower fluxes at solar maximum.

2.4.3 Geomagnetic field

The Earth is protected from cosmic rays by a magnetic field. It is a dipole-field that interacts with and is shaped by the flow of plasma from the sun. The transition where this *geomagnetic field* starts to dominate is called the *magnetopause* and is the boundary of the Earth's *magnetosphere*. The flow of plasma from the sun creates a termination shock ahead of the magnetopause in the direction facing the sun. At the opposite side, the plasma forms a *magneto tail*. The geomagnetic field shields off low-energy particles but is also influenced by solar activity leading to charged particles penetrating deeper into the magnetosphere during solar events.

Charged particles can get trapped in the field, which causes two radiation belts consisting of cosmic ray particles to form around the earth. These radiation belts do not reach into the atmosphere, except at polar regions and at the South Atlantic anomaly. Therefore, they pose no threat to atmospheric balloon missions at lower latitudes.

The *outer radiation belt* consists of trapped high-energy plasma and is influenced by the solar activity. This belt reaches low altitudes in the polar regions where is less shielding from solar activities by the geomagnetic field, forming the *polar horns*. The intensity and the geographic extent of the polar horns varies at times with increased solar activity.

The *inner belt* contains trapped protons having energies up to a few hundred MeV. The proton flux at low altitudes varies with the solar cycle. At solar maximum, the atmosphere expands due to the grater insolation and more protons are lost in the atmosphere.

2.5 Neutron background production in the atmosphere

2.5.1 Description

Neutrons are produced as secondary particles in the atmosphere by charged primaries [12]. Because of this the neutrons inherit properties of the charged cosmic rays regarding flux and variation due to solar activity. SPEs thus cause significant neutron fluxes in the atmosphere.

When cosmic rays hit the atmosphere they may interact with atmospheric nuclei in two different ways that lead to production of neutrons as secondary particles. Low energy neutrons, with energies less than about 10 MeV, are mostly produced in evaporation of excited nuclei and tend to have an isotropic angular distribution. *Evaporation* is a process in which a nucleus is excited by an energetic particle to a high temperature with a subsequent disintegration that produces neutrons, protons and alpha particles. This is somewhat similar to *knock-off* or *spallation* reactions, in which fragments of a nuclei are ejected due to impact of an energetic projectile. The neutrons produced have insufficient energy to disintegrate further nuclei and are slowed down in the atmosphere by elastic and inelastic collisions with oxygen and nitrogen nuclei, for instance in the $^{14}\mathrm{N}(n,p)^{14}\mathrm{C}$ reaction [13]. High energy neutrons can be knocked off in collisions or in charge exchange reactions with particles of high energy and have an anisotropic distribution. These may have energies reaching those of the primaries.

At high altitudes, *albedo neutrons* can be scattered out of the atmosphere which contributes to the upwards neutron flux. If the albedo neutrons decay in the radiation belts, the resulting protons will be trapped there [14]. At balloon altitudes, which are above most of the atmospheric mass (at 36 km altitude the overburden is 5 g/cm^2 compared to 58 g/cm^2 at 20 km) the majority of the neutrons are produced at a lower altitude.

2.5.2 Neutron spectrum

Calculated as well as measured neutron spectra for various atmospheric depths are shown in figures 3.2 and 3.3. The implemented neutron spectrum model will be introduced in chapter 3.

The neutron spectrum starts with roughly a $1/E$ energy dependence for energies below 10 keV. This is exact shape if the scattering cross section is independent of energy but due to absorption and energy dependent cross section the spectrum has to be approximated by a $1/E^{\alpha}$ energy dependence. From 1 eV to 50 keV the energy dependence of the neutron flux is $\phi(E) \propto 1/E^{0.88}$. At about 1 MeV, which is the energy of the produced evaporation neutrons, the spectrum is modified again. This is the evaporation peak. In the region 10 MeV to 500 MeV the spectrum shows a steeper falloff [14][1].

2.6 Scintillators

Scintillators are materials that respond to radiation by *fluorescence*, which is excitation followed by emission of visible light. The radiation detectors employed in PoGOLite are based on two different types of scintillators. A good description of the function of scintillators can be found in literature [8, 9].

Organic scintillators that are used in PoGOLite are based on plastic polymers. The molecular structure of organic scintillators results in π-bonds being formed by electrons. These can be excited by radiation which results in emission of light upon de-excitation.

The energy levels of such a molecule are illustrated in figure 2.4, where singlet states are labeled as $S_0, S_1, S_2, \ldots$ and triplet states are labeled as $T_0, T_1, T_2, \ldots$ Vibrational sub levels are labeled as $S_{00}, S_{01}, \ldots$ A passing charged particle excites an electron to a higher energy state. The higher singlet states are de-excited within orders of picoseconds to the S_1 state while vibrational energy is lost due to thermalisation. The excitation thus results in molecules ending up in the S_{10} state. De-excitation from this state to a lower results in fluorescence, and is the main component of scintillation light.

Through a transition called *inter-system crossing* a singlet state may be converted to a triplet state. The lifetime of the triplet state is three orders of magnitude longer than of a singlet state which causes a delayed light emission called *phosphorescence*.

An important feature of a scintillator is that it should be transparent to its own emission. Since some of the transitions from the S_{10} energy level are to a vibrational sub-level of the S_1 state they represent a lower energy than the minimum required for excitation and the fluorescence light can not re-excite the molecule.

Not all de-excitations lead to emission of visible light but result in the excitation energy being converted to heat, which is referred to as *quenching*.

Inorganic scintillators, such as BGO, which is used in PoGOLite, get their scintillation properties by a crystal lattice structure where the electrons are restricted to certain energy bands. The lower energy band, called the *valence band*, is populated by electrons bound to a specific atom in the crystal lattice. The electrons can be excited to the *conduction band* where they are free to move throughout the crystal leaving a hole that also is free to move. Electrons and holes can also move together in a configuration called an *exciton*.

Impurities called *activators* are added in order to create energy levels below the conduction band since a de-excitation from the conduction band to the valence band would result in a photon with too high energy to be visible. A free hole that encounters an activator can

---

[1] The conclusions therein are for aircraft altitudes and below but the qualitative description should still be applicable.

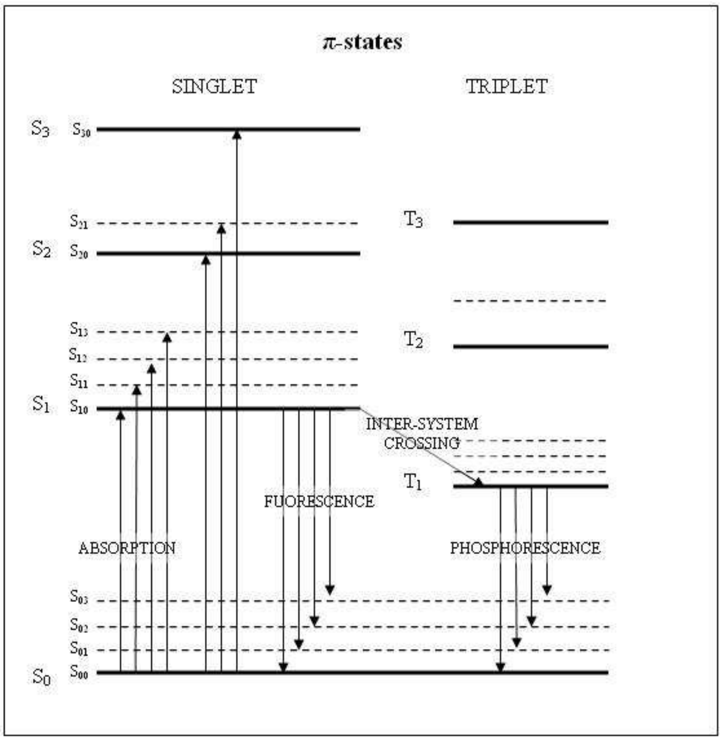

Figure 2.4: Energy levels of an organic molecule with π-electron structure. From [15].

ionize the atom at that site because the ionization energy of the impurity is less than that of a lattice site. A following excited electron can then be captured by the hole at the activator site and make transition to the ground state. There is a high probability that a photon is emitted at this de-excitation, however radiation-less transitions that contribute to quenching are also possible.

Since the energy of transition at an activator site is less than the energy of excitation the emission spectrum is shifted towards longer wavelengths and the emission is not affected by re-absorption. If the transition to the ground level at the activator site is forbidden the electron will require further excitation before a de-excitation to the ground state is possible, which results in phosphorescence.

With some exceptions, the response time of inorganic scintillators is longer than that of organic scintillators.

The amount of phosphorescence and the decay time of scintillation light is dependent upon the type of particle or radiation that excites the scintillator. This makes it possible to distinguish different types of radiation by analysis of the resulting pulse shape. However, it will not be possible to use this method on PoGOLite to distinguish neutron interactions since scintillators with different response times are used. Also, neutron interactions may lead to gammas being created as secondary particles.

2.7 Photomultipliers

Photomultiplier tubes, or *photomultipliers* are used for the registration of light emitted by the scintillators. A schematic of a photomultiplier is shown in figure 2.5. The principle of function of a photomultiplier relies on the *photoelectric effect* by which incoming photons release electrons in the *photocatode*, which are then passed on to the electron-multiplier stage.

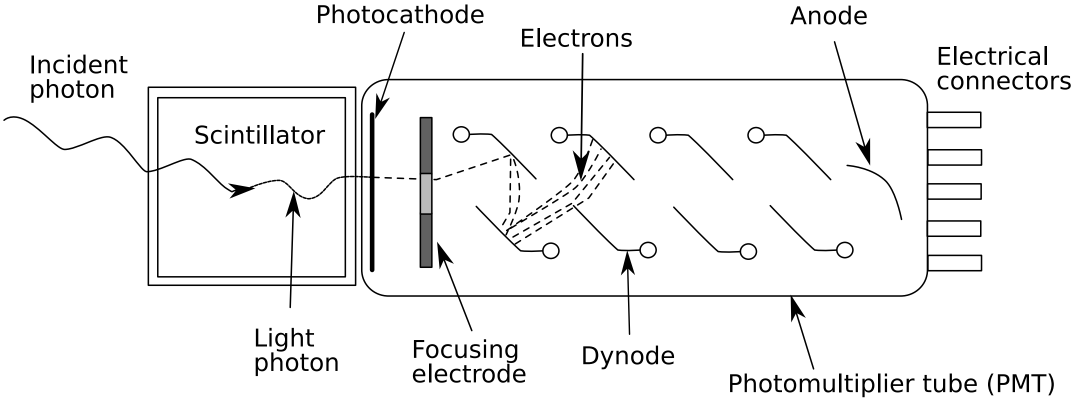

Figure 2.5: Schematic of a photomultiplier tube coupled to a scintillator. From [16]

An incoming photon that hits the photocatode may be absorbed and transfer its energy to an electron. In order for the electron to escape, it must migrate to the surface of the material and there have sufficient energy to escape. The energy of the electron emitted at the photocatode can be expressed as

$$E = h\nu - \phi, \tag{2.8}$$

where E is the kinetic energy of the emitted electron and ν is the frequency of incident light. ϕ is the work function, which is the threshold energy required to release an electron from the material. For typical light emitted from a scintillator, $h\nu$ is about 3 eV while the work function can be 1.5 eV for semiconducting materials or 3 eV and higher, depending on material [8]. The probability for this effect to take place varies with the frequency of the incident light. The efficiency of a photocathode is expressed by the *quantum efficiency*, QE, which is dependent on the frequency of the incoming light and is defined as

$$\mathrm{QE}(\lambda) = \frac{\text{number of photoelectrons emitted}}{\text{number of incident photons}}, \tag{2.9}$$

where λ is the wavelength of the incoming light. In practice, QE can be 20% to 30% [8].

After emission from the photocatode the electrons are collected and focused onto the first dynode of the electron-multiplier stage by an electric field created by a system of focusing electrodes. The electron current is amplified by *secondary emission*, a process similar to the photoelectric effect where an electron takes on the role of the incoming photon. An electron that collides with a dynode transfers its energy to the dynode material which emits a number of secondary electrons that can release further electrons at the following dynode. The dynodes are held at a decreasing electric potential in order to maintain an electric field that accelerates and guides the electrons. At the end of the electron-multiplier an electron current is read out at the anode and can be further processed by electronic means. Gains of 10^7 can be obtained [9]. The signal at the anode depends on the number of electrons created at the photocathode. Ideally, the amplification should be linear (independent of energy).

Chapter 3

Simulation

3.1 Software

Geant4 [17] is a toolkit for simulation of particle interactions in matter, based on the Monte Carlo method [18]. It is a set of software libraries, written in C++ and is a result of a collaboration between a large group of physicists and software experts. It contains "an abundant set of physics models to handle the interactions of particles in matter" and "incorporates a large part of what is known about particle interactions" [17]. The modular structure means that the user can construct a program at compile time with components from the toolkit and self-supplied.

All the physical interactions of cosmic ray particles are simulated in a program that is built on components from the Geant4 framework. The implementation of code that simulates PoGOLite consists of definitions of the geometry and materials of the detector, a physics list and several definitions of cosmic ray sources and backgrounds. Geant4 version 8.2.p01[1] was used for the simulations.

ROOT is an object-oriented framework for large data analysis that includes functions for statistical analysis and visualisation [19]. In this work ROOT is used to produce plots of the data and for some analysis related to those plots.

3.2 Simulation model

Prior to the work presented here different types of cosmic rays had been simulated with the detector design and the program [20] used for those studies is also used here. Provided were classes for generation of cosmic ray particles with implementation of a spectrum and flux which served as a base for implementing a neutron spectrum. Much of the code used for analysis was inherited from the studies of energy dependent polarisation [21].

Different setups of the PoGOLite detector were simulated. As the simulations of the originally proposed design showed a significant contribution to background from neutrons a new measure to block neutrons was tested. This came in the form of a polyethylene shield surrounding the side and back of the detector. This was simulated at first with a thickness of 5 cm and, as the final design, with a thickness of 10 cm on the side and 15 cm in the bottom. There was also a concern that a significant contribution to background could come from neutrons induced in the gondola structure supporting the detector, as had been shown in a

---

[1] NDL 3.10, CLHEP 2.0.3.1

previous balloon experiment [22]. Therefore, a simulation was made with protons incoming on a hollow aluminium sphere surrounding PoGOLite. The results of these simulations are presented in the next chapter.

3.2.1 PoGOLite model

The implementation of the geometric layout of the detectors was used without modification to that used in previous studies [20].

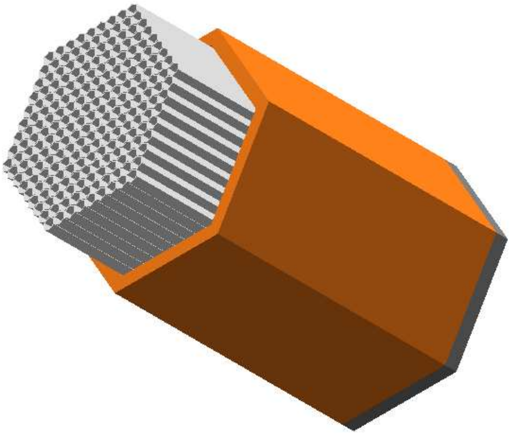

Figure 3.1: Graphic representations of the simulated PoGOLite model.

An object in Geant4 is defined as a geometrical shape in space to which a material with physical properties is assigned. The materials are defined by the relative mass content of the types of atoms, density and pressure.

The slow and fast scintillators of the PDCs are both simulated by the same material, *plastic*. The bottom shield and the side shield are simulated as *BGO*. The side shield is defined as a single piece with straight inner surfaces whereas the actual design will consist of several individual scintillators that on the inward side closely follows the shape of the adjacent PDCs. The PMTs and supporting structure is not defined in the simulation.

3.2.2 Physics list

The processes that Geant4 uses when tracking particles in a simulation must be defined in a *physics list*.

The physics list that was provided from the previous simulation included only specific processes that were needed then and none for neutron interactions. Instead of defining the required processes by hand the Geant4-provided physics list QGSP_BERT_HP was used. This physics list “uses a quark gluon string model for projectile interacting with nuclei and a pre-equilibrium decay model with an extensive evaporation phase to model the fragmentation of the nucleus 'after the punch'. Below 3 GeV the Bertini cascade is used for nucleon and pion induced reactions.” [23]. Among the processes used for neutrons can be mentioned: ionisation, decay, elastic and inelastic processes.

3.2.3 Neutron spectrum

The code for the generation of primary neutrons was based on the code used for generation of the primary gamma background. The spectrum is defined by power-law functions of the form

$$f_i(E) = A_i E^{a_i} \tag{3.1}$$

on sub-intervals over the energy range, where f_i is flux from sub-interval i and E is energy. A_i and a_i are fitting constants, these were obtained by fitting straight lines to (log-log) plots of calculations of neutron background shown in figures 3.2 and 3.3. These figures were chosen because they contain measured values together with a continuous calculated spectrum. Four sub-intervals were used for the neutron spectrum. The figures used for the fitting were obtained by calculation and describes omnidirectional differential neutron spectrum at an atmospheric depth of 5 g/cm^2, which corresponds to an altitude of 36 km, for solar minimum and geomagnetic[2] latitude 42° N [24]. The corresponding geographic latitude is at the level of the Mediterranean and the middle of the USA.

The energy ranges of the sub-intervals are shown in table 3.1 together with their contribution to the total flux. The resulting model spectrum is shown in figure 3.4.

sub-interval	from	to	flux from this region [neutrons/s/cm^2]	A_i	a_i
1	1 keV	1 MeV	0.4925	0.104	-0.884
2	1 MeV	15 MeV	0.2121	0.100	-1.189
3	15 MeV	70 MeV	0.1454	0.0135	-0.450
4	70 MeV	1 GeV	0.1640	3.135	-1.732
1 - 4	1 keV	1 GeV	1.014		

Table 3.1: The sub-intervals on which fits to the atmospheric neutron spectrum were made and their contribution to the flux.

The differential spectrum is used as a probability distribution when a neutron energy is randomized. Before the simulation starts, the integrals of the functions over the energy sub-intervals are calculated analytically as well as the integral of the whole spectrum. Since the differential spectrum has unit of cm^{-1}s^{-1}MeV^{-1} the integral will describe the flux in unit cm^{-1}s^{-1} from the energy range integrated.

The energy is randomized by first choosing one of the sub-intervals, i, with a probability proportional to the flux from that interval relative to the total flux. By treating (3.1) as a frequency function of a random distribution, a random energy is obtained by the relation

$$E = F_i^{-1}(R) = (\frac{a_i + 1}{A_i} R)^{\frac{1}{a_i+1}} \tag{3.2}$$

where F_i is the distribution function associated with (3.1) so that $F_i'(x) = f_i(x)$ and F_i^{-1} is its inverse function. R is a random number from a flat distribution on the range of the selected $F_i(E)$.

3.2.4 Generation of initial tracks

In each event in the simulation one neutron is assigned an energy and direction vector and then tracked along its path interacting with the materials it encounters.

---

[2] This refers to the axis of the Earth's magnetic field. This is different from the geographic axis since the geomagnetic field is tilted relative to the rotation axis of the Earth.

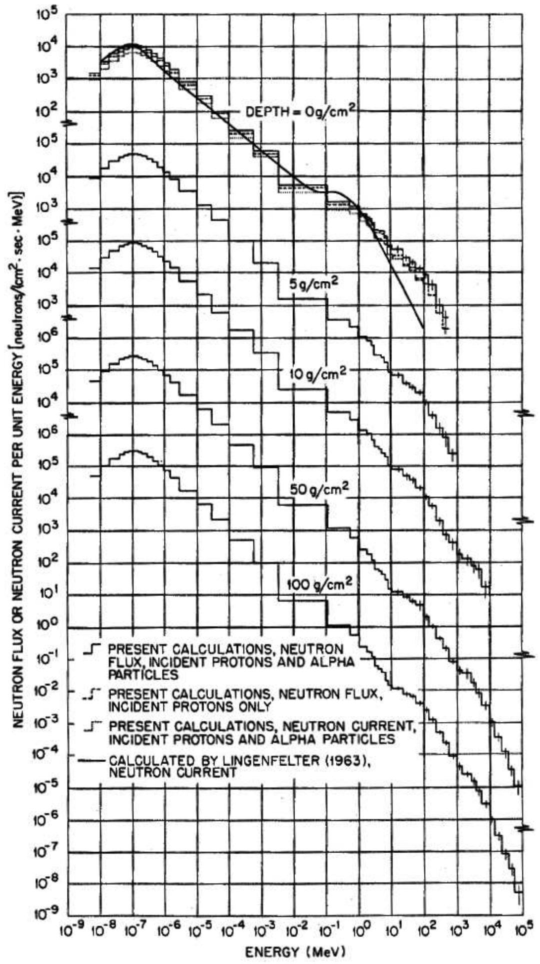

Figure 3.2: Neutron spectra at various depths from the top of the atmosphere as presented in [24]. Solar minimum, latitude 42°N.

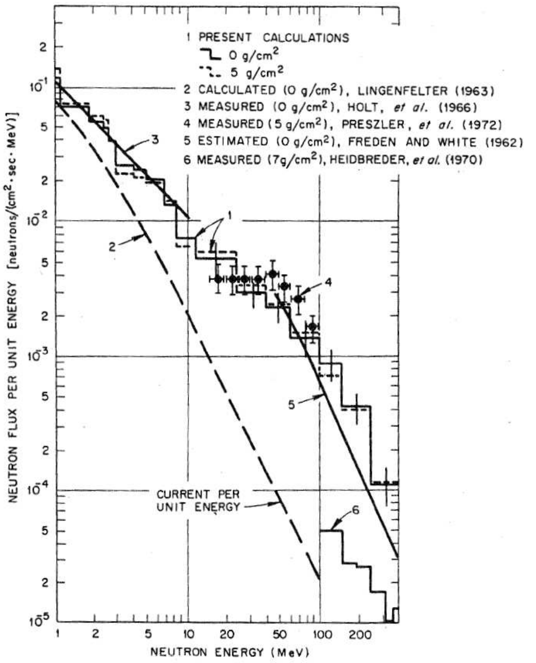

Figure 3.3: Neutron spectra near the top of the atmosphere as presented in [24].

The initial track is created by generating a momentum vector with all directions equally probable. The azimuth and polar angles of the initial particles momentum vector are randomly chosen according to

$$\begin{aligned} \phi &= 2\pi R_{(0,1)} \\ \theta &= \cos^{-1}(R_{(-1,1)}), \end{aligned} \tag{3.3}$$

where R_I denotes a random number from a flat distribution on the interval I. Thus $\phi \in (0, 2\pi)$ and $\theta \in (0, \pi)$ with an isotropic angular distribution. While the azimuth angle ϕ of the momentum vector can be chosen from a flat distribution, the polar angle θ must be chosen proportionally to a differential area element at θ on the unit sphere. The track is then offset randomly in a plane perpendicular to the momentum vector by a value up to the length of the detector so that all parts have a chance to be hit.

Figure 3.5 describes this process in two steps. A position is chosen at a distance d from the

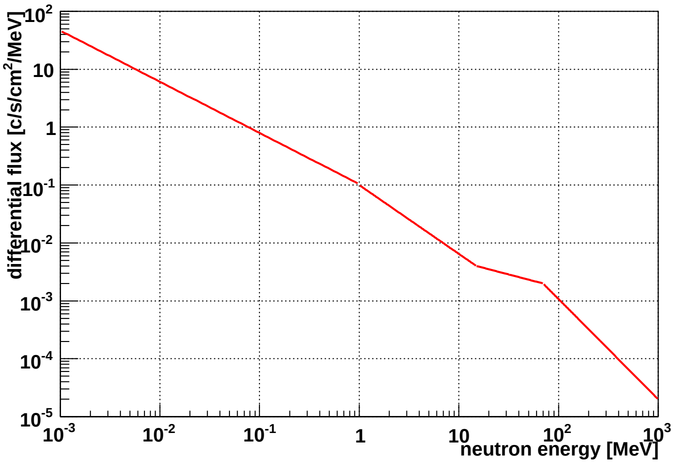

Figure 3.4: The modeled neutron flux.

midpoint of PoGOLite, O, where d is equal to the length of PoGOLite. The offset coordinates in the xy-plane, x_{off} and y_{off} are randomly chosen randomly so that $x_{\mathrm{off}}^2 + y_{\mathrm{off}}^2$ can be as large as up to half the length of PoGOLite. The area in which the offset takes place represents a source area for the neutron flux. The frame of the initial track is then rotated around the y- and z-axes by the angles θ and ϕ obtained as described above. The initial track can then be generated from the source point S and with a momentum vector in the direction of AO. This way all of PoGOLite can be covered by neutrons.

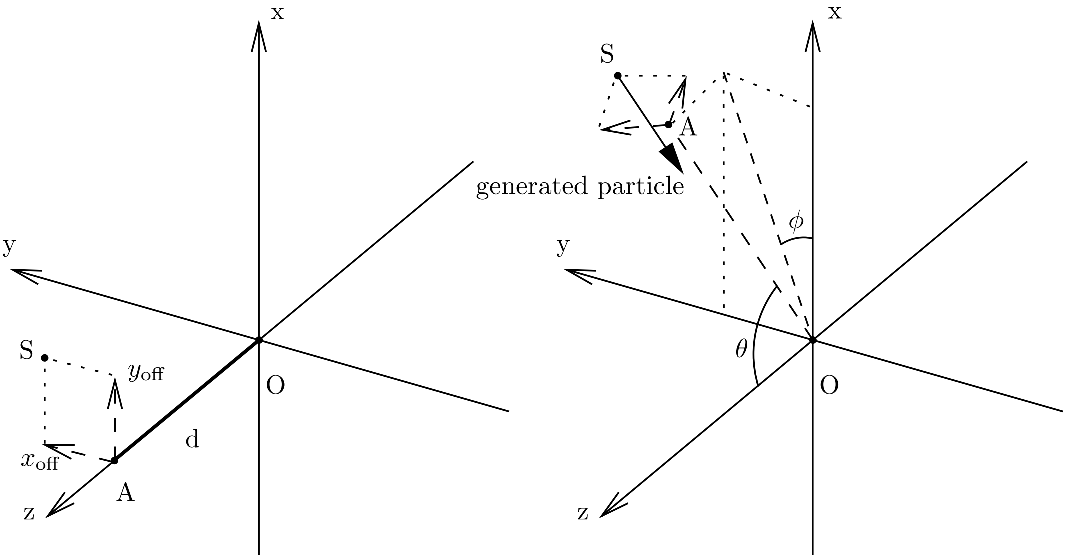

Figure 3.5: Generation of the initial tracks in two steps. Left: the offsets in x and y are chosen, right: the coordinate system of the momentum vector is rotated around point O. The momentum vector is generated from the source point S and is parallel to AO.

The initial tracks are always pointing inwards, towards PoGOLite. This means that only half the actual flux is generated (the flux going outwards would miss the detector anyway), which must taken into consideration when calculating the total flux.

The spatial distribution being generated is omnidirectional whereas in [22] it is mentioned that 80% of the flux is directed upwards. The direction of observation may however vary and by treating all directions equally there is also a possibility to examine the directional sensitivity of the detector. The information about the initial particle is saved in each event so there is a possibility to re evaluate the spatial distribution during later analysis.

3.2.5 Estimation of instrument response

In the simulation, the total energy deposition in each type of detector as well as cell number is recorded. Thus the determination of which part of the PDC that has been hit is made directly and not by analysis of pulse shape as will be done in during the actual measurements. The light yield and PMT response is not simulated in the Geant4 program although the deposited energy is altered to give the effect of a reduced light yield due to quenching. The total energy deposition is recorded also for the bottom and side shield detectors.

The quenching process was added to the geant4 simulation. Upon deposition of energy by a proton or a nucleus in a fast or slow type of scintillator the deposited energy was changed to mimic a lower light output. The measured light yield L [MeVee][3] for protons is given by [25, 26]

$$\begin{array}{ll} L = 0.0478 \cdot E_p + 0.0432 \cdot E_p^2 & , E_p < 10\text{MeV} \\ L = 0.859 \cdot E_p - 2.971 \cdot (1.0 - \exp(-0.20 \cdot E_p)) - 1.2 & , E_p > 10\text{MeV}, \end{array} \tag{3.4}$$

where E_p [MeV] is the proton energy. For nuclei, the relation (3.4) is used divided by 10 [27].

For each event that leads to a hit in a detector a line with information about which detectors were hit and the energy deposited in each detector is added to an output file[4].

This, however, is not the energy that would be seen when looking at the output from the photo multipliers. A step, called *reduction*, is performed in order to simulate the instrument response. This is done by processing the output file of the Geant4 simulation and produces another output file. During this step all events that do not produce precisely two or three hits in the fast scintillators are discarded. The energies deposited in the fast scintillators are then *smeared*, modified by a random value, according to a Gaussian distribution and a detection threshold of 2 keV is applied. This implements the limitations and accuracy of a PMT.

The distance, in units of detector width, between the detectors that register the biggest and the second biggest energy deposition is also calculated, which corresponds to a photo absorption and a Compton scattering. Also calculated is the azimuth angle between these hits, which can be used for polarisation studies, and the polar and azimuth angles of the initial track is passed on to the output file as well.

3.3 Data analysis

The reduction step leaves information that is processed further to give the estimated measured spectra.

---

[3] MeV electron equivalent. By definition, to generate 1 MeVee a fast electron with an energy of 1 MeV is required but heavy charged particles require a higher energy due to their reduced light yield.

[4] This is a modification from the original program which only saved this information if a fast scintillator had been hit.

Plots are produced that show the measured flux of neutrons before and after application of the veto and with a Compton kinematics cut. These are compared to fluxes from a 100 mCrab accreting pulsar and total gamma background with the veto system applied.

The veto system is in this analysis triggered by an energy deposition exceeding 100 keV in any of the fast plastic, side shield BGO or bottom BGO detectors. In that case the event is not counted.

The spectra are plotted in histograms which have varying bin widths due to the log-scale. In order to convert counts to detected flux the bins of the histogram are scaled by multiplication with the factor

$$\frac{F_{\text{tot}}}{N_{\text{events}}\Delta E_{\text{bin}}} \cdot \frac{A_{\text{source}}}{A_{\text{geom}}} \tag{3.5}$$

where F_{tot} [counts/s/cm^2] is the integral of the generated differential flux taken over energy, N_{events} is the number of generated events, ΔE_{bin} [keV] is the energy range of the bin, A_{source} [cm^2] is the area which the initial particles are spread on and A_{geom} [cm^2] is the area of the surface that the initial particles hit. This is based on the scaling method used in the program `modan.cc` that has been used in previous simulation studies of PoGOLite [21].

The area terms in the scaling appear from the fact that not all particles that are generated will be aimed at and hit the detector assembly. The value of A_{geom} that is used in the analysis is 934.5 cm^2, which approximates the frontal cross-section area of the fast scintillators. Since neutron background is detected by not only the front area of PoGOLite this scaling will not show the actual flux of neutrons but rather the perceived flux as compared to the flux of the observation source.

Chapter 4

Results

4.1 Simulation of the original design

4.1.1 Measured flux

Figure 4.1 and 4.2 shows the calculated background levels as would be seen by PoGOLite. $5 \cdot 10^6$ events have been simulated. The simulated neutron spectrum in figure 4.1 is isotropic and is defined as described in chapter 3. Figure 4.2 shows the case where 80% of the neutrons are moving upwards and assuming the z-axis of PoGOLite is pointing in the zenith direction. This has been obtained by re-weighting the events with according to the direction of the initial neutron. Figures 4.3 and 4.4 show a close-up view in the region 20 keV–200 keV, which is the region of interest for triggering of PoGOLite, of figures 4.1 and 4.2 respectively. The data from the simulation has been processed by reduction and smearing so the events shown are those where two or three fast detectors have given a signal above the threshold value.

A reference 100 mCrab spectrum is shown for comparison, this is obtained by simulating an accreting pulsar with a spectrum given by

$$\phi = 0.0473E^{-1.1} \cdot \exp(-E/70), \tag{4.1}$$

where ϕ [c/s/cm^2/keV] is the differential flux and E [keV] the energy on the range from 20 keV to 200 keV. Also shown is a gamma background spectrum obtained in a simulation similar to the one used for neutrons here. The data for the 100 mCrab and the gamma background spectrum were simulated elsewhere [21].

There are three curves showing a neutron spectrum in figures 4.1 and 4.2. All of these adopt a selection criteria that there is an energy deposition above a threshold in two or three fast scintillators. The *before vetoing* plot shows the spectrum as it would be seen by the detector when hits in the veto system are ignored. The *after vetoing* plot shows the flux as it would be seen when events in which there is a signal from any veto detector have been discarded. In the *veto & Compton kinematics* plot there is an additional requirement that the highest energy deposition in a fast scintillator is within 20 keV and 100 keV (corresponding to photo-absorption) and the second highest within 1 keV and 15 keV (corresponding to a Compton scattering).

As can be seen, the measured flux from neutron background is significantly higher than gamma background and exceeds the 100 mCrab level. This was unexpected as previous work had assumed that the gamma background dominated and a 100 mCrab signal could be detected.

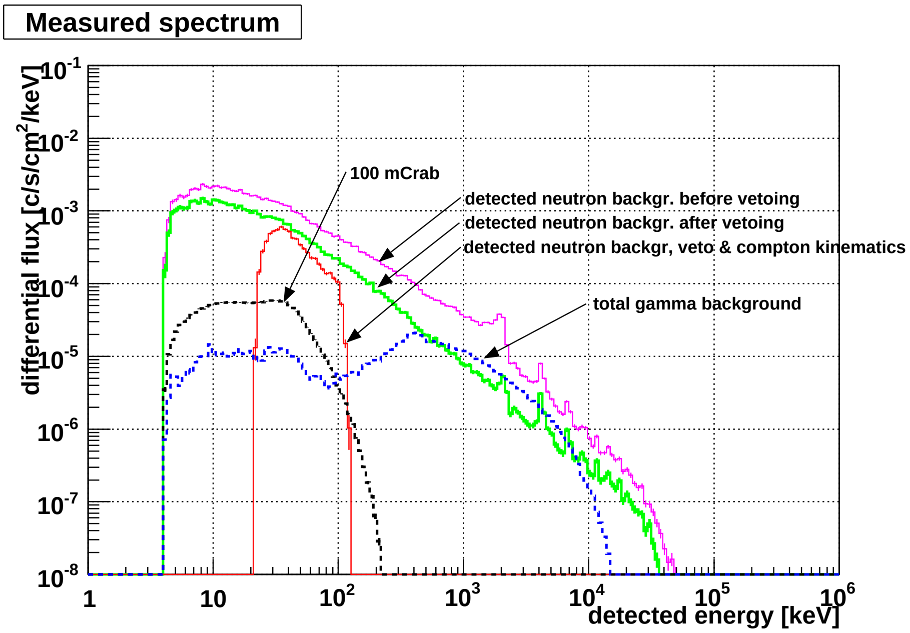

Figure 4.1: The simulated contribution to background radiation as measured by the detector. Isotropic spectrum

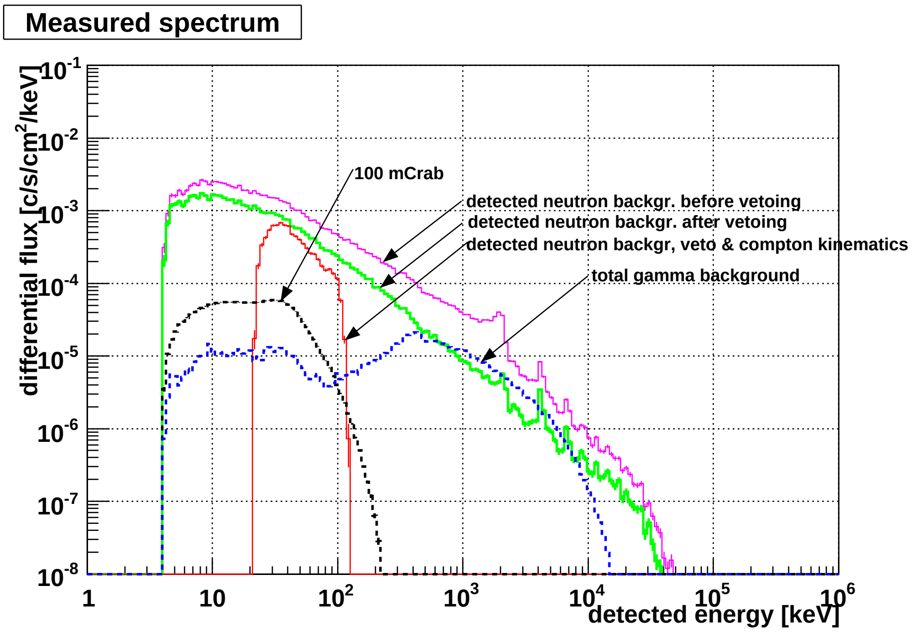

Figure 4.2: The simulated contribution to background radiation as measured by the detector. The spectrum here has been re-weighted so that 80% of the neutrons are moving upwards.

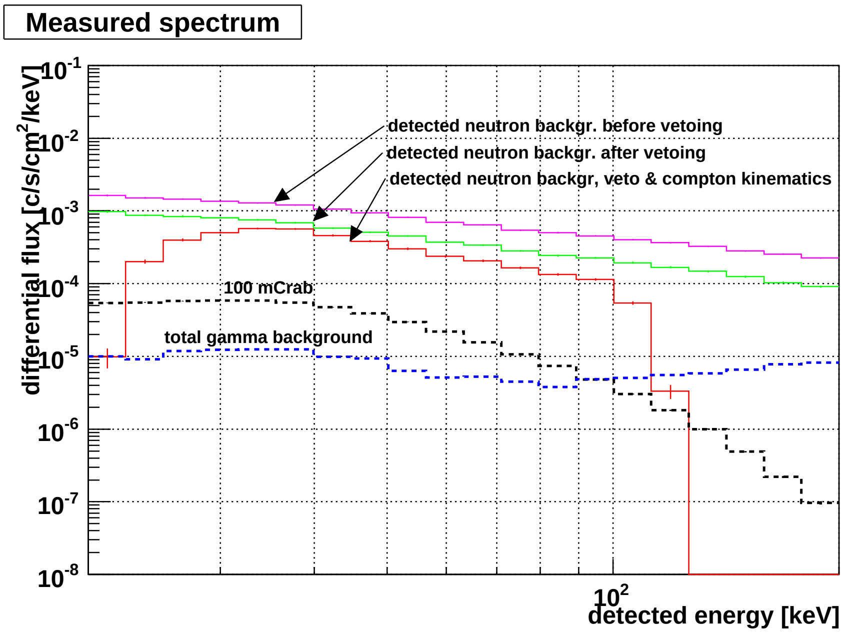

Figure 4.3: Close-up view of figure 4.1 in the region 20 keV–200 keV.

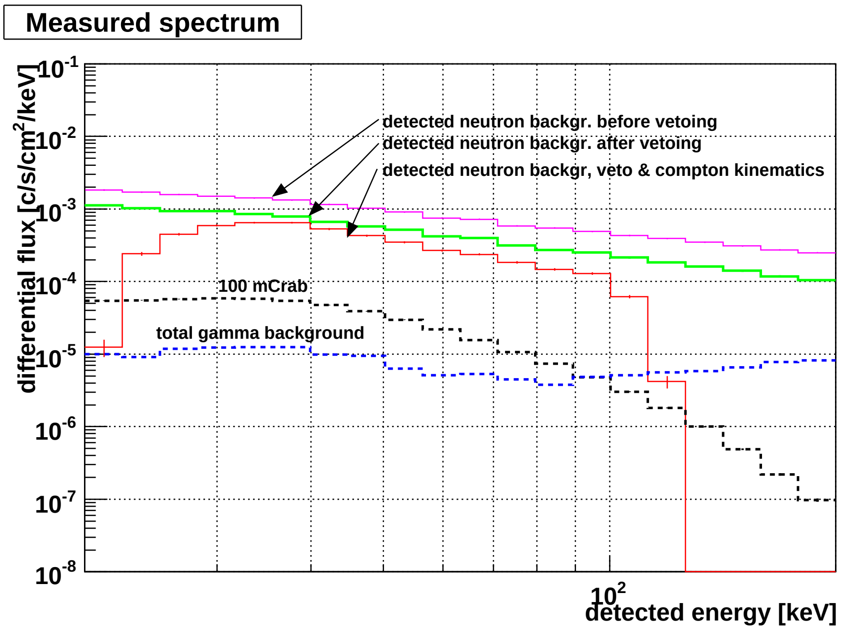

Figure 4.4: Close-up view of figure 4.2 in the region 20 keV–200 keV.

The contributions to flux are summarized in table 4.1 which shows integrated values of the corresponding plots in figure 4.3.

	total flux [counts/s/cm^2]	event rate [counts/s]
neutrons without vetoing	0.01757	16.42
neutrons with vetoing	0.01000	9.346
neutrons with Compton kinematics	0.004929	4.606
100 mCrab	0.0005217	0.4876
gamma background	0.0001052	0.09831

Table 4.1: Total flux and event rate for an isotropic neutron spectrum, gamma background and the 100 mCrab source. The values for 100 mCrab and gamma background are taken after applying the veto system and should be compared to the values of the neutron background with vetoing.

4.1.2 Directional dependency

It is important to try to reduce the neutron background. An insight into the mechanisms by which neutrons interact with the detectors in PoGOLite can be obtained by examining the directional dependency of the measured events.

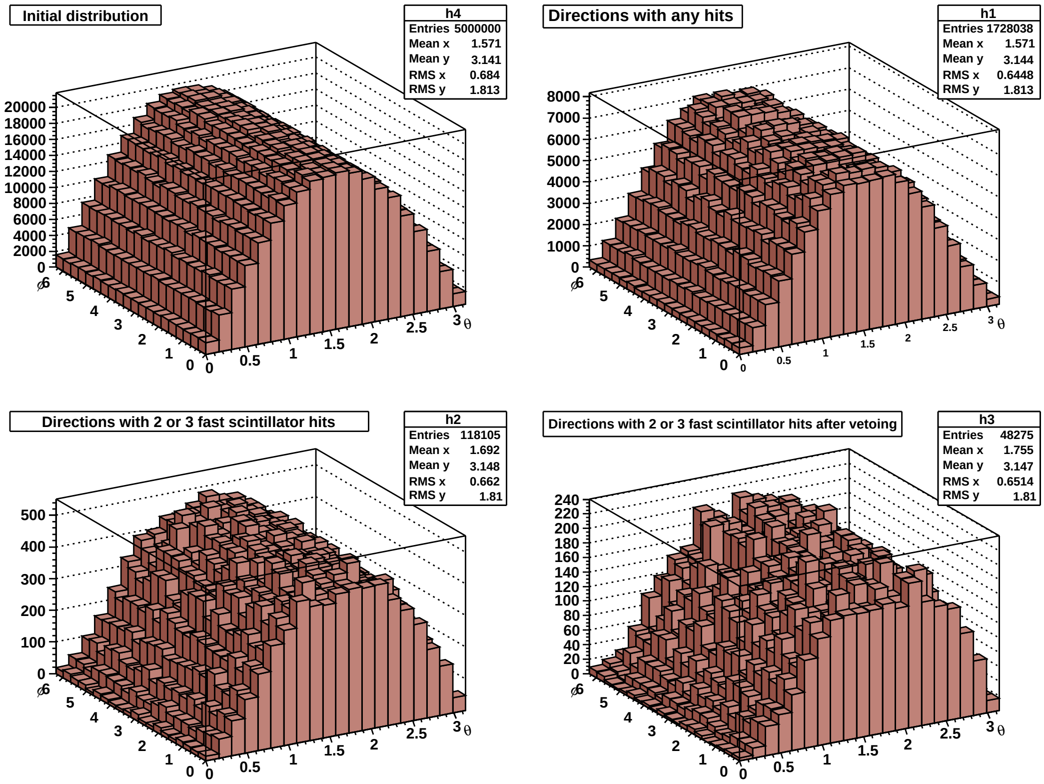

Figure 4.5: Events versus the θ and ϕ coordinates of the momentum vector of the generated neutron. Note that the bins do not correspond to a constant spatial angle. Top left: the initial distribution as generated in the Geant4 simulation. Top right: events that lead to energy deposition in a detector of any type. Bottom left and right: events that give two or three hits in the fast scintillators, without and with vetoing applied respectively.

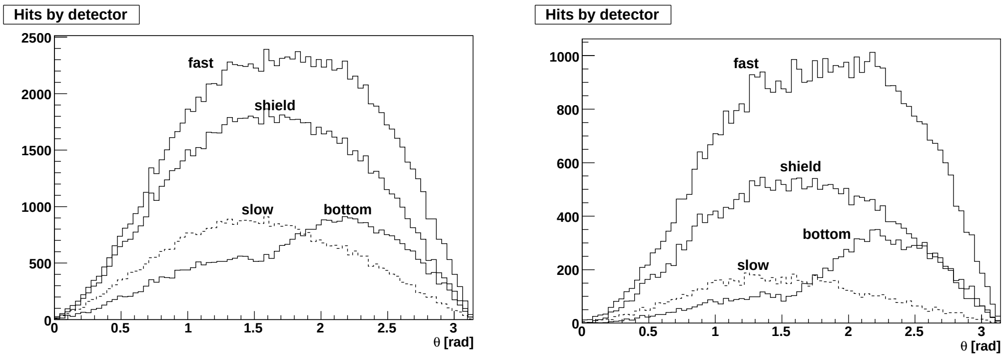

Figure 4.6: Events versus the θ angle of the generated neutron registered by each individual type of detector in events where two or three fast scintillator detectors are hit. Left: regardless of vetoing, right: events with veto signal removed.

Figure 4.5 shows the number of events versus the direction of the momentum vector of the initial neutron. The polar angle θ is the angle to the z-axis, where $\theta = 0$ means the neutron is moving from top to bottom through the detector assembly parallel to the z-axis, and ϕ is the azimuth angle. The bins in these histograms do not represent spatial regions of the same size. For instance, at $\theta = 0$ and $\theta = \pi$ the direction is the same regardless of the angle ϕ.

The top two histograms of figure 4.5 are based on data coming directly from the Geant4 simulation and before the smearing process has been performed. The top left histogram shows the generated momentum vectors of the neutrons shot onto the detector. The distribution is omnidirectional and not dependent on the energy of the neutron. The top right histogram shows for which directions there was a deposition of energy in any of the detectors. This can give an estimation of how many of the generated events that are aimed at the detector assembly. There is the possibility that a neutron will pass through without interacting, these events are not counted here.

The bottom two histograms show the initial directions that leads to energy deposition in two or three fast scintillators. The effect of the veto discrimination can be seen in the bottom right histogram where events leading to a detected signal in the veto system have been discarded. Veto discrimination is activated in events where there is a detection in one of slow scintillators, the bottom BGO scintillators or the side shield meaning that some energy can have been scattered out of the detector or that incoming particle did not originate from the intended source.

It is useful to note that the total amount of entries presented in each histogram. Of the $5 \cdot 10^6$ events generated, $1.72 \cdot 10^6$ events or 34% are estimated to be aimed at the detector assembly. Of these, 6.8% give hits in two or three detectors before vetoing and 2.3% after.

Figure 4.5 shows only a negligible variation along the ϕ-axis. (A small variation in detected events comes from the fact that the cross section area of PoGOLite varies when looking from the side due to the hexagonal design). However, the shape along the θ-axis in the detected events differs from the initial distribution. An additional insight may be gained by looking at the directional dependency for each type of detector. Figure 4.6 shows the dependency on the angle θ on the initial track for the different types of detectors in events where two or three fast scintillator detectors are hit. For each event a count is recorded for each type of detector if any detector of that type is hit. The data sets for the fast detectors of these histograms correspond to the bottom histograms of figure 4.5.

These figures show that there is a larger proportion of hits in the bottom BGO detectors for tracks coming into the rear hemisphere of PoGOLite ($\theta > \pi/2$) than for track coming in from the frontal hemisphere. A similar feature can also be noted for the fast plastic scintillators. By observing individual events during the Geant4 simulation it can be seen that neutrons may scatter inelastically in BGO, producing secondary gammas that can enter the fast plastic scintillators. This may explain the increase for the fast scintillators that follows the bump of the bottom detectors. Plastic scintillators are more effective at absorbing the neutrons. Since there is a block of plastic scintillators in front of the bottom BGO detectors they are shielded from neutrons entering from the front, which explains the relatively lower amount of hits from that direction.

4.1.3 Spatial distribution

More information can be extracted by studying the number of hits induced by neutron events in each PDC ring[1]. Table 4.2 shows the distribution of valid events registered for each PDC ring of PoGOLite, where ring 1 is the central cell and ring 9 consists of the outermost cells. It is clearly seen that the probability of registering an in incoming neutron is higher for an outer ring than for a layer closer to the center. This can be explained since the outer rings are more exposed and that they are located closer to the BGO shield.

ring	number of detectors in ring	hits	hits per detector
1	1	334	334
2	6	2100	350
3	12	4202	350
4	18	6677	371
5	24	9229	385
6	30	13345	445
7	36	20430	568
8	42	41356	985
9	48	73515	1532

Table 4.2: Distribution of hits in layers of PoGOLite. Counted here are events where two or three fast scintillators are hit and no hits in the veto system are detected.

Figure 4.7 shows the spacing between the biggest registered hits for events with two or three hits and no detection in the veto system. The two hits correspond to the supposed photo absorption and Compton scattering events that are used for calculating the polarisation angle. The distance shown is relative to the spacing of adjacent detector cells (for instance the distance between the midpoints of the cells). To make comparing between simulations with differing amounts of generated events possible the data in presented in terms of proportion to the total amounts of events registered in that simulation. Note that the distance between two cells not adjacent to each other is not necessarily an integer although the histogram is binned so.

This figure shows that neutron events give hits that tend to be more contained than gamma events, which is backed up by the fact that there are more neutron induced hits in the outer rings than in the inner. This can be explained since neutrons give hits by inelastic scatterings in the BGO shields that induce gamma particles that in turn are detected. Thus, in the worst case, the outer rings can be used as an extra anticoincidence shield.

---

[1] A group of PDCs whose midpoints share the same hexagon centered on the detector assembly.

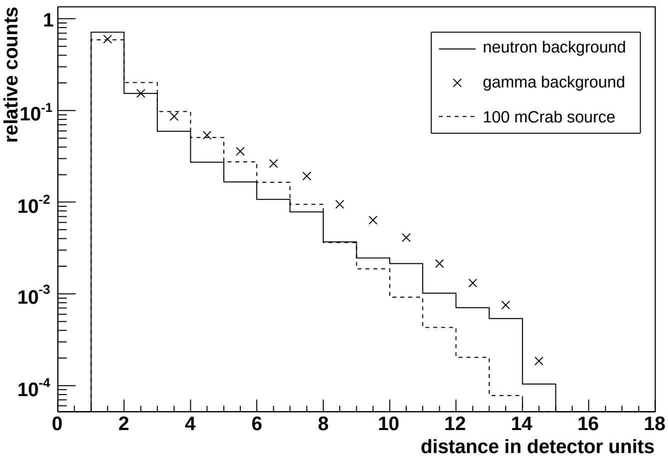

Figure 4.7: Distribution of distance between the two detector cells with the largest energy depositions in events with two or three hits registered by the fast detectors and no veto signal. The length unit used is the distance between adjacent detector cells. Counts are presented as relative to the total number of counts registered.

4.2 Simulation with 5 cm polyethylene shield

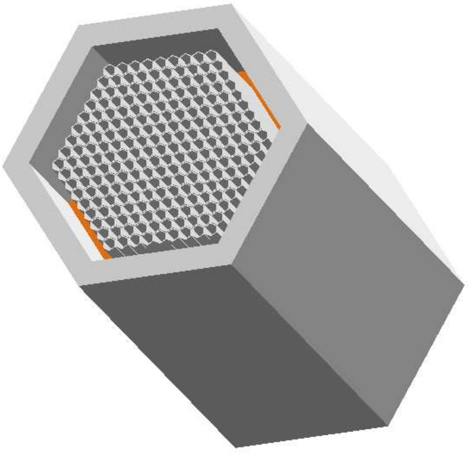

Figure 4.8: PoGOLite with a 5 cm polyethylene shield.

The simulation of PoGOLite has revealed that it will be too sensitive to the neutron background and that the anticoincidence system will not be effective against it. As a measure of passive shielding against the neutron background, a plastic shield can be introduced. Plastic has a high hydrogen content, which with its light mass is good at absorbing the kinetic energy of incident neutrons through elastic scatterings (see section 2.2.2).

A 5 cm thick polyethylene shield on the sides and back was added to the model of PoGOLite. The simulated model is shown in figure 4.8. In the actual simulation this shield was made of paraffin, with a hydrogen to carbon atom ratio of 42 to 20 and a density of 0.93 g/cm^3 A total of $5 \cdot 10^6$ events were simulated. Figures 4.9 through 4.12 show the measured flux for this design in a similar way to figures 4.1 through 4.4. The values of the integrated fluxes in the region 20 keV – 200 keV are shown in table 4.3.

What can be seen is that the polyethylene does provide some protection against the neutron background. Also, the effect of the veto system seems to increase. This lowers the neutron background but not enough, it is still higher than the 100 mCrab level.

	total flux [counts/s/cm^2]	event rate [counts/s]
without vetoing	0.007400	6.916
with vetoing	0.001841	1.721
with Compton kinematics	0.0008958	0.8371
100 mCrab	0.0005217	0.4876
gamma background	0.0001052	0.09831

Table 4.3: Total flux and event rate from backgrounds and the 100 mCrab source in the region 20 keV – 200 keV. The values for 100 mCrab and gamma background are taken after applying the veto system and should be compared to the values of the neutron background with vetoing.

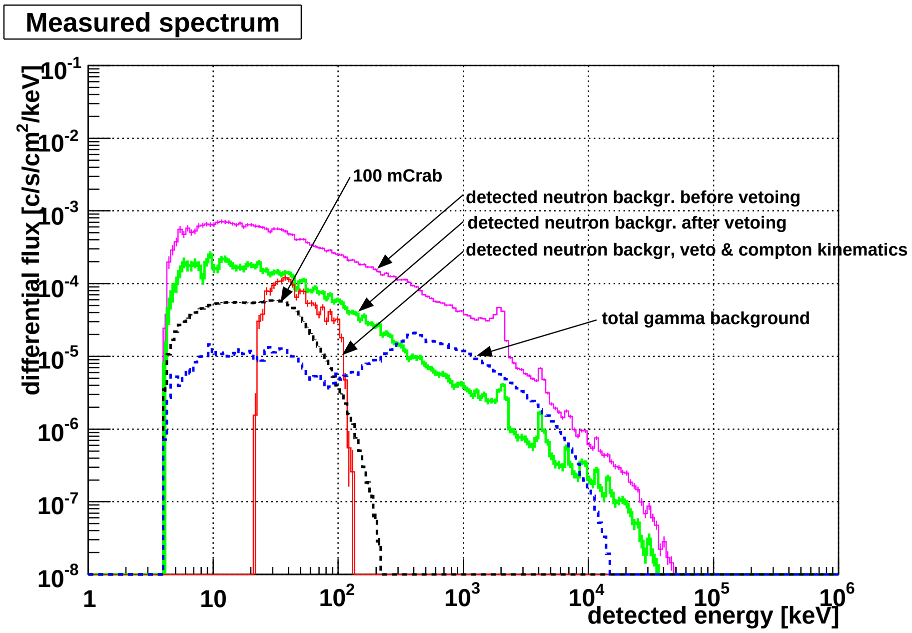

Figure 4.9: The simulated contribution to background radiation as measured by the detector. Isotropic spectrum and with a 5 cm polyethylene shield.

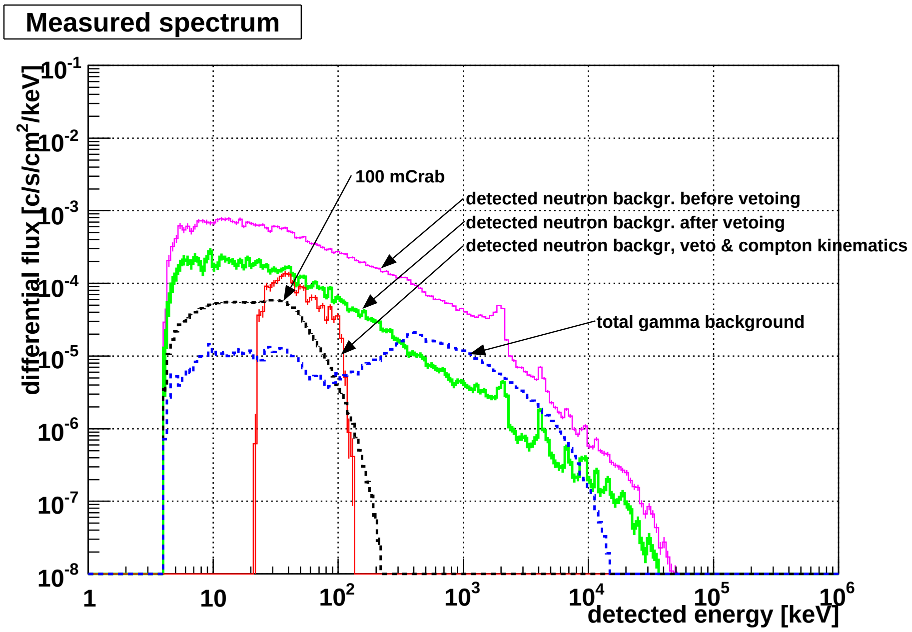

Figure 4.10: The simulated contribution to background radiation as measured by the detector. The spectrum here has been re-weighted so that 80% of the neutrons are moving upwards.

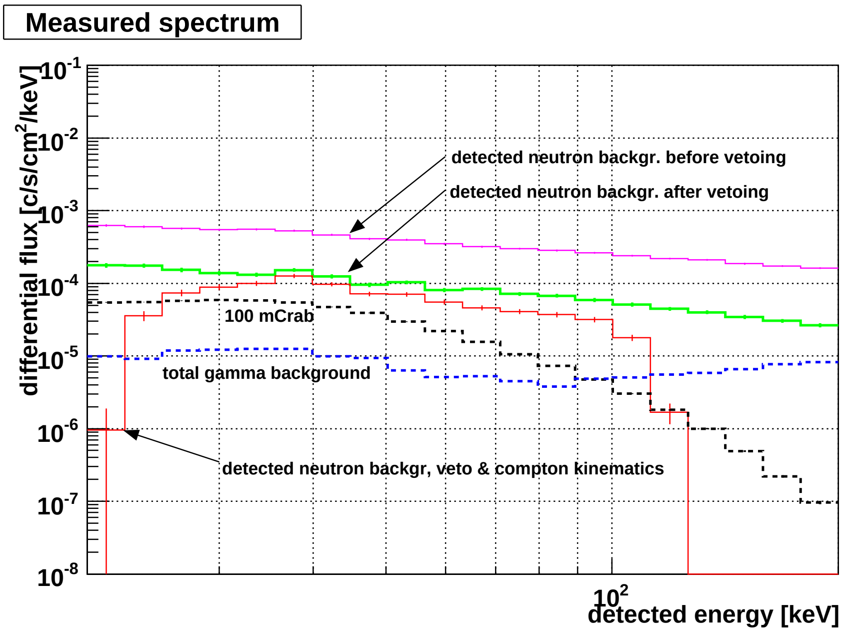

Figure 4.11: Close-up view of figure 4.9 in the region 20 keV–200 keV.

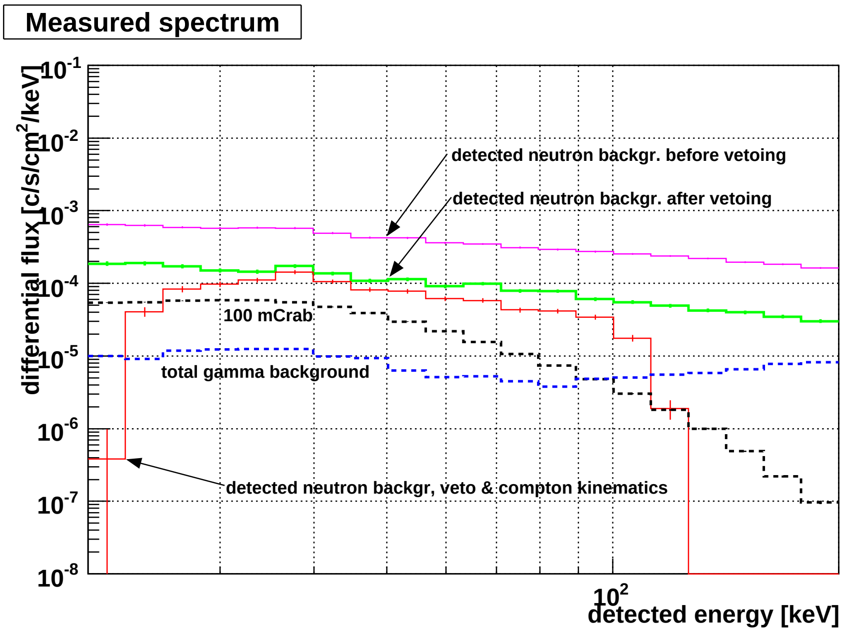

Figure 4.12: Close-up view of figure 4.10 in the region 20 keV–200 keV.

4.3 10 cm side and 15 cm bottom polyethylene shield

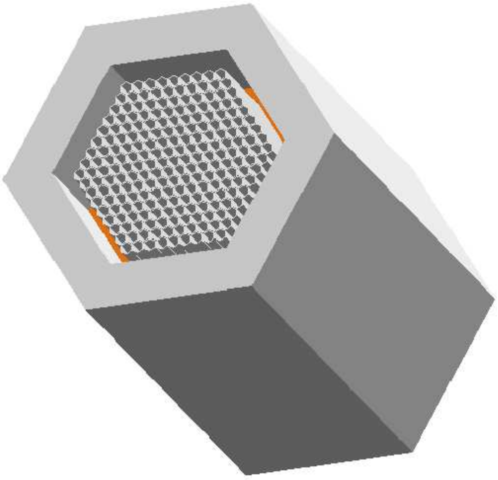

Figure 4.13: PoGOLite with a polyethylene shield of 10 cm thickness at the sides and 15 cm in the bottom.

In this design a polyethylene shell with a thickness of 10 cm on the side and 15 cm in the bottom as shown in figure 4.13 was added to PoGOLite. The results of this simulation are shown in figures 4.14 through 4.17 and in table 4.4 in a similar way as presented in the previous sections.

	total flux [counts/s/cm^2]	event rate [counts/s]
without vetoing	0.005025	4.696
with vetoing	0.0005143	0.4807
with Compton kinematics	0.0002522	0.2357
100 mCrab	0.0005217	0.4876
gamma background	0.0001052	0.09831

Table 4.4: Total flux and event rate from backgrounds and the 100 mCrab source. The values for 100 mCrab and gamma background are taken after applying the veto system and should be compared to the values of the neutron background with vetoing. With polyethylene shield.

It can be seen that the number of neutrons that produce hits in the fast scintillators are less than in the simulation presented in the previous section. Also, the effectiveness of the veto system increase further. The neutron flux is now suppressed below the 100 mCrab level at energies below 70 keV.

A similar analysis to the one in sections 4.1.2 and 4.1.3 of the directional sensitivity and the relative distances between neutron induced hits is shown in figure 4.18 and table 4.5. The sensitivity to neutrons entering from the back of the detector is smaller than previously and also neutron induced hits are more evenly spread out on the detector rings. The increased effectiveness of the veto system suggests that incoming neutrons are moderated by the polyethylene shield to energies that are more easily detected.

Evaluations of different polyethylene wall thicknesses done within the PoGOLite collaboration has shown that increasing the wall thickness further will result in a lesser decrease of

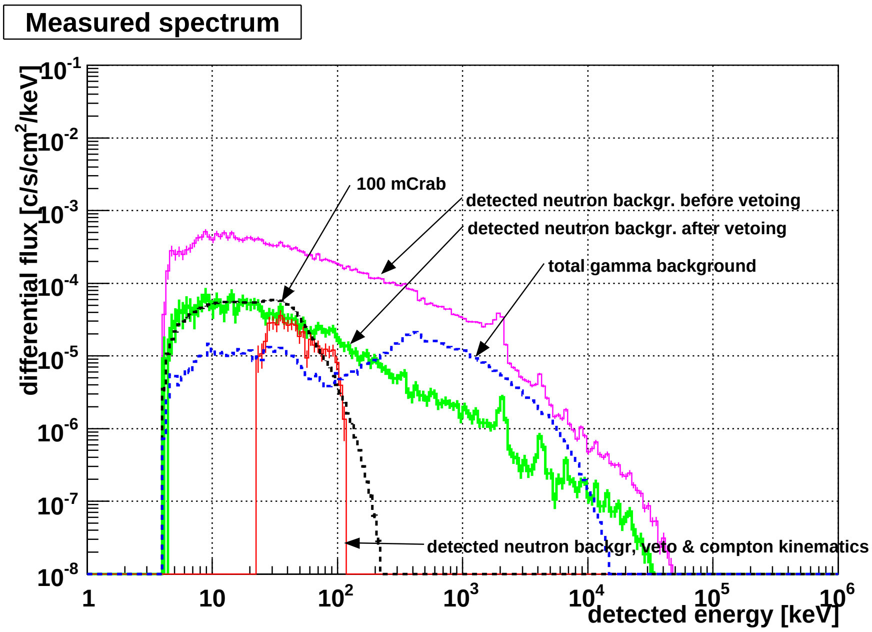

Figure 4.14: The simulated contribution to background radiation as measured by the detector. Isotropic spectrum and with a 10 cm polyethylene shield.

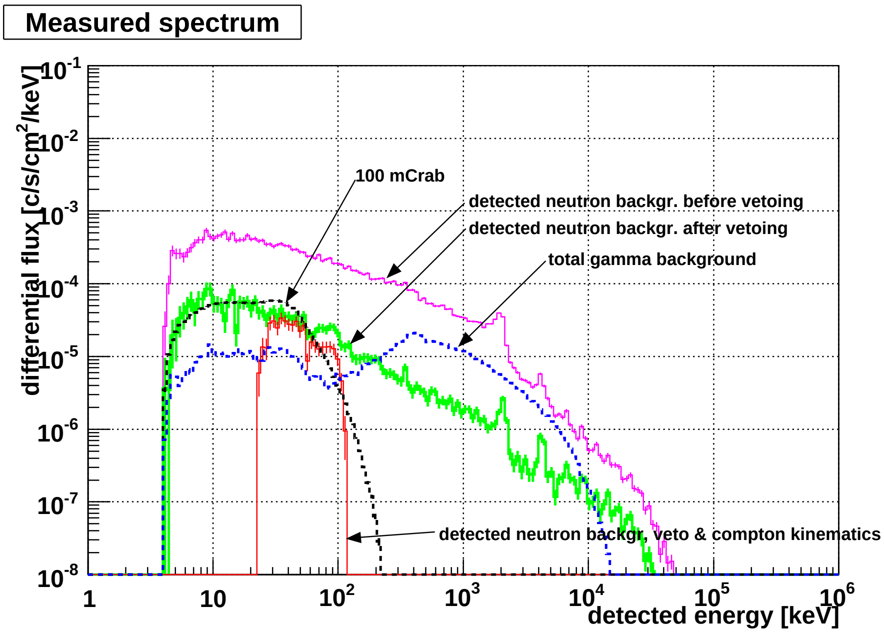

Figure 4.15: The simulated contribution to background radiation as measured by the detector. The spectrum here has been re-weighted so that 80% of the neutrons are moving upwards.

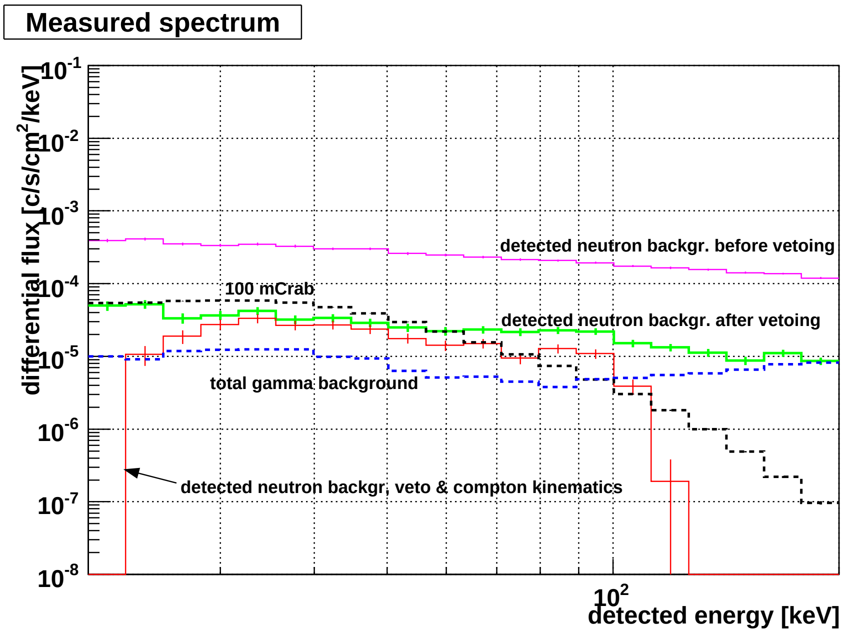

Figure 4.16: Close-up view of figure 4.14 in the region 20 keV–200 keV.

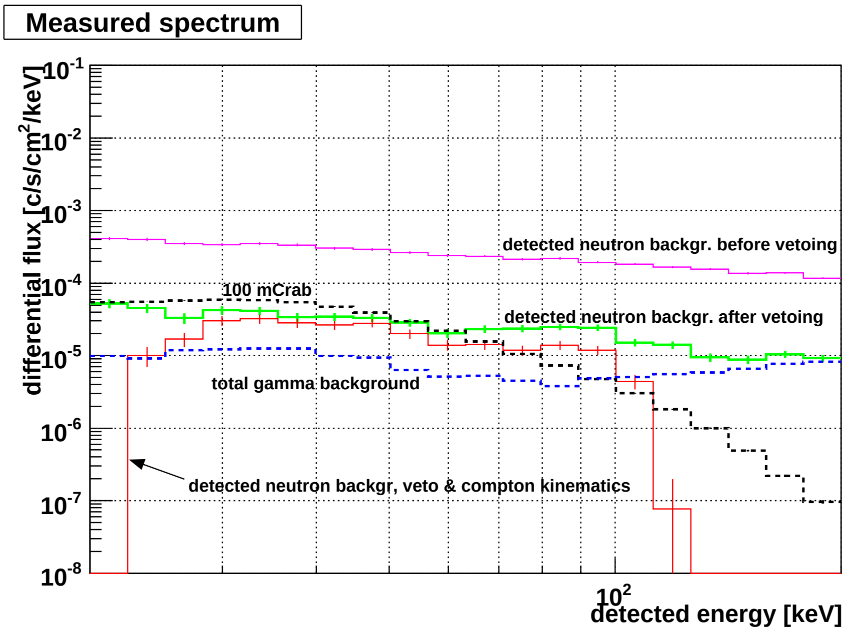

Figure 4.17: Close-up view of figure 4.15 in the region 20 keV–200 keV.

the neutron background. The actual weight of the polyethylene shield would be about 200 kg, one do not want to add more weight if it is not necessary.

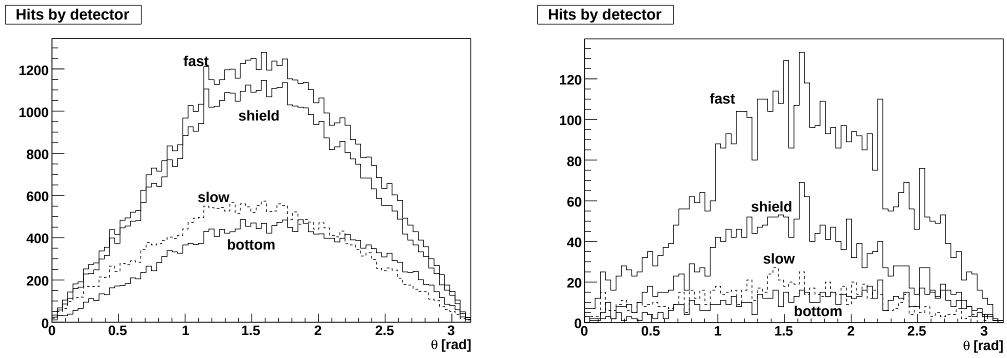

Figure 4.18: Events versus the θ angle of the generated neutron registered by each individual type of detector in events where two or three fast scintillator detectors are hit. With polyethylene shield. Left: regardless of vetoing, right: events with veto signal removed.

Layer	number of detectors	hits	hits per detector
1	1	35	35
2	6	217	36.2
3	12	471	39.3
4	18	615	34.2
5	24	1008	42.0
6	30	1302	43.4
7	36	1835	51.0
8	42	2143	51.0
9	48	2276	47.4

Table 4.5: Distribution of hits in layers of PoGOLite with polyethylene shield. Counted here are events where two or three fast scintillators are hit and no hits in the veto system are detected.

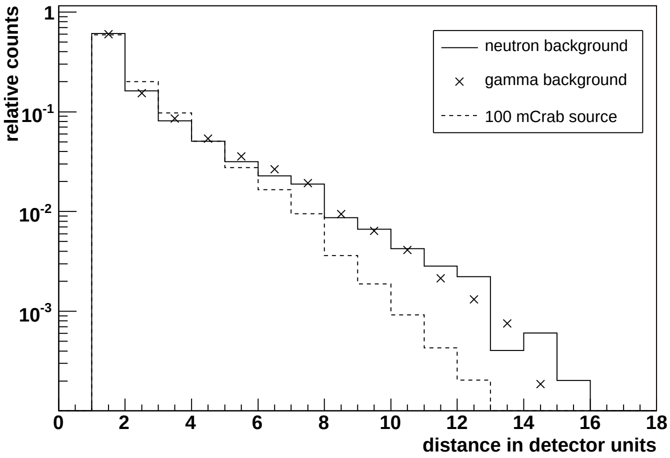

Figure 4.19: Distribution of distance between the two biggest hits in events with two or three hits registered by the fast detectors and no veto signal. The length unit used is the distance between adjacent detector cells. Counts are presented as relative to the total number of counts registered.

4.4 Simulation of neutrons induced in aluminium structure

Neutrons can be produced in nuclear reactions by cosmic ray protons that hit the gondola structure supporting PoGOLite. Interactions of protons with the supporting structure were simulated by representing the structure by a spherical aluminium shell with a thickness of 3 cm surrounding PoGOLite. The secondary particles are not limited to neutrons only. One may consider this study as an indication of proton induced background.

The proton spectrum that was used was already present in the PoGOLite simulation program [20, 28]. This spectrum is highly anisotropic, with most protons coming in from the frontal hemisphere of the detector since it in this simulation is oriented upwards with the z-axis pointing in the zenith direction.

The results of a simulation with $3 \cdot 10^6$ protons generated are shown in figures 4.20 and 4.21. The flux of the simulated protons is 367.5 [protons/s/m^2]. The resulting flux of proton induced background, after considering the veto system, is $1.23 \cdot 10^{-5}$ counts/s/cm^2 or 0.0115 counts/s.

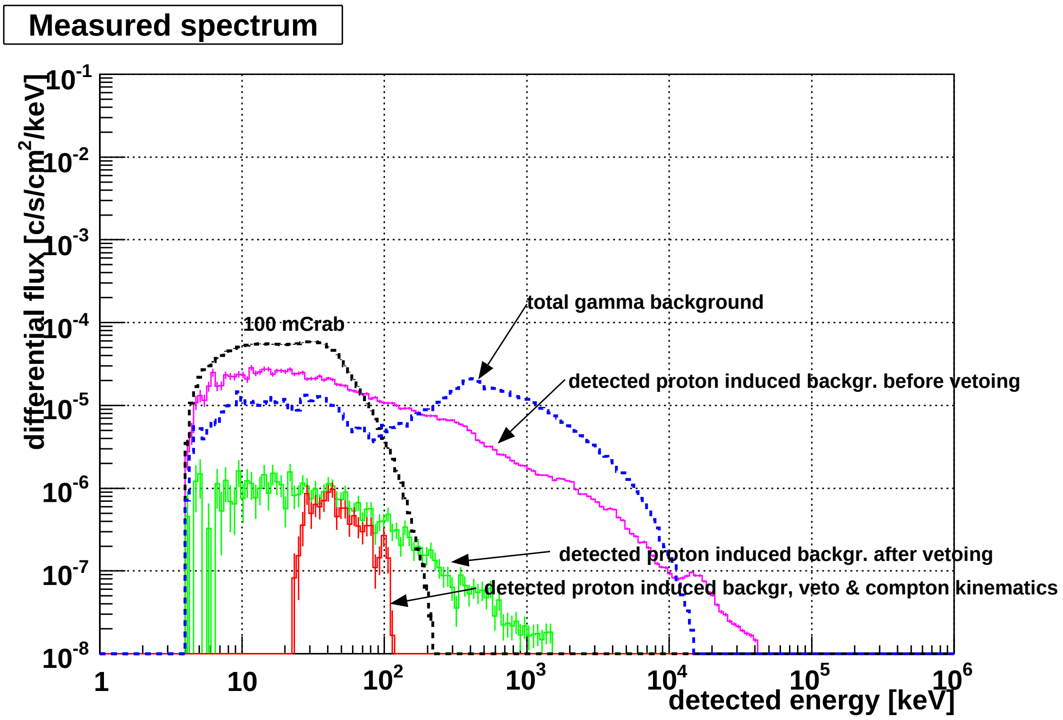

Figure 4.20: The measured spectra by radiation induced by protons in a 3 cm thick aluminium shell surrounding PoGOLite.

The figures show that the contribution to background by protons hitting surrounding aluminium material is much smaller than the other backgrounds. The same conclusion has been drawn from analytic calculations [2].

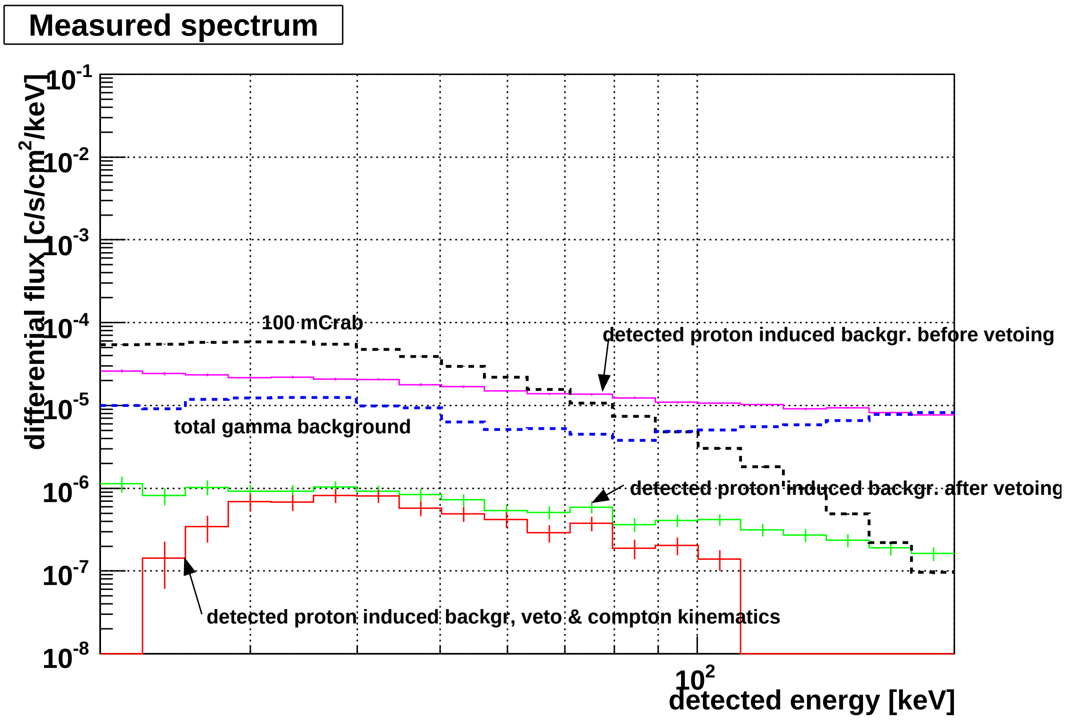

Figure 4.21: Close-up view of figure 4.20 in the region 20 keV – 200 keV.

Chapter 5

Conclusions

The results of this study have shown that atmospheric neutrons can introduce a significant background to observations with PoGOLite and may set the limit on the flux level and energy range that can be observed. The anticoincidence shield of PoGOLite was not effective in reducing the neutron background. As a result of this study a passive shield of polyethylene is introduced in the design. This shield proves to be successful at blocking and moderating neutrons. The polyethylene shield also has the effect of making the anticoincidence system more effective, so that PoGOLite is able to meet the observational design goals.

The impact of this study on the final design is visible in figure 5.1, where polyethylene shielding is seen.

Launches of PoGOLite have been proposed from Palestine, Texas and Kiruna in northern Sweden. In this study, an atmospheric neutron spectrum for a geomagnetic latitude of 42° N has been assumed. This may describe the neutron background environment for the launch site in Palestine well but not certainly so for the Kiruna site, as the neutron flux varies with the latitude [12].

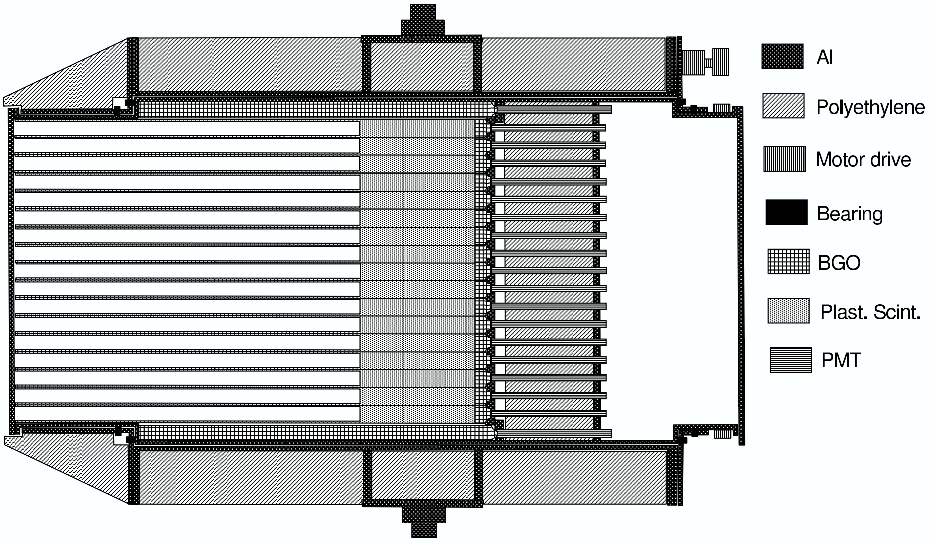

Figure 5.1: Cut-through drawing of the PoGOLite detector assembly.

Appendix A

Coordinate system

The coordinate system used in the simulation and in this report is shown in figure A.1. The z-axis runs along the detector parallel to the detector cells and is positive from bottom to top. The definitions of the polar angle θ and the azimuthal angle ϕ are also shown in figure A.1. The orientation of this coordinate system is fixed to the detector. For instance, the z-axis does not necessarily point in the zenith direction. As an example, a photon originating from the observed target will have a momentum vector with a negative z-direction and θ close to zero.

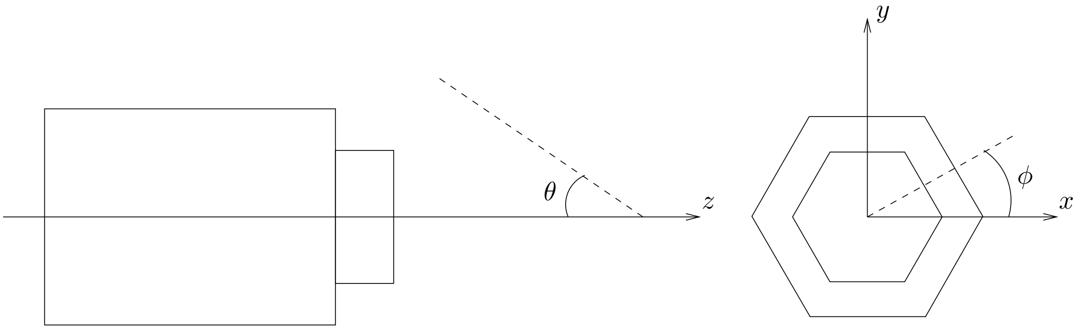

Figure A.1: Definition of the coordinate system. Left is a view from the side with the z-axis positive from bottom to top of the detector assembly. To the right the detector is shown as seen from the top.

Acknowledgments

I would like to thank my supervisor Professor Mark Pearce for supporting me and giving me a great opportunity to work on the PoGOLite project at the Royal Institute of Technology (KTH) in Sweden. It has been exciting to work together with The PoGOLite collaboration and the people at the Particle and Astroparticle Physics group at KTH. I would like to thank Tsuneyoshi Kamae, Tsunefumi Mizuno, Wlodzimierz Klamra, Stefan Larsson and all others who came with ideas and suggestions for my work, and Olle Engdegård for helping me with starting using the PoGOLite code.

Bibliography

[1] M.C. Weisskopf, G.G. Cohen, H.L. Kestenbaum, K.S. Long, R. Novick, and R.S. Wolff. Measurement of the X-ray polarization of the Crab Nebula. *Astrophysical Journal*, 208(pt 2):L125–L128, 1976.

[2] T. Kamae et al. The PoGOLite Soft Gamma-ray Polarimeter. Submitted to *Astronomy and Astrophysics*, August 2007.

[3] S.J. Sturner, C.D. Dermer, and F.C. Michel. Magnetic Compton-induced pair cascade model for gamma-ray pulsars. *The Astrophysical Journal*, 445:736, 1995.

[4] J.K. Daugherty and A.K. Harding. Gamma-Ray Pulsars: Emission from Extended Polar CAP Cascades. *The Astrophysical Journal*, 458:278, 1996.

[5] K.S. Cheng, C. Ho, and M. Ruderman. Energetic Radiation from Rapidly Spinning Pulsars. I. Outer Magnetosphere Gaps. *Astrophysical Journal*, 300:500–521, 1986.

[6] PoGOLite - Swedish Consortium Homepage. `http://www.particle.kth.se/pogolite/` Accessed August 27, 2007.

[7] A. J. Dean, F. Lei, and P. J. Knight. Background in space-borne low-energy gamma-ray telescopes. *Space Science Reviews*, 57:109–186, 1991.

[8] Glenn F. Knoll. *Radiation Detection and Measurment.* John Wiley & Sons, Inc, 3 rd. edition, 2000.

[9] W. R. Leo. *Techniques for Nuclear and Particle Physics Experiments.* Springer-Verlag, 1987.

[10] T. Mizuno, T. Kamae, JST Ng, H. Tajima, JW Mitchell, R. Streitmatter, RC Fernholz, E. Groth, and Y. Fukazawa. Beam Test of a Prototype Detector Array for the PoGO Astronomical Hard X-ray/Soft Gamma-ray Polarimeter. *Nuclear Inst. and Methods in Physics Research, A*, 540(1):158–168, 2005.

[11] M. Dikpati, G. de Toma, and P.A. Gilman. Predicting the strength of solar cycle 24 using a flux-transport dynamo-based tool. *Geophys. Res. Lett*, 33(10.1029), 2006.

[12] J.A. Simpson. Neutrons Produced in the Atmosphere by the Cosmic Radiations. *Physical Review*, 83(6):1175–1188, 1951.

[13] H.A. Bethe and G. Placzek. On the Interpretation of Neutron Measurements in Cosmic Radiation. *Physical Review*, 57(7):573–587, 1940.

[14] W.N. Hess, H.W. Patterson, and R. Wallace. Cosmic-Ray Neutron Energy Spectrum. *Physical Review*, 116(2):445–457, 1959.

[15] Wikipedia, the free encyclopedia.
`http://upload.wikimedia.org/wikipedia/en/6/61/Pistates.jpg`
Accessed May 28, 2007.

[16] Wikipedia, the free encyclopedia.
`http://en.wikipedia.org/wiki/Image:Photomultipliertube.svg`
Accessed May 30, 2007.

[17] S. Agostinelli, J. Allison, K. Amako, J. Apostolakis, H. Araujo, P. Arce, M. Asai, D. Axen, S. Banerjee, G. Barrand, et al. Geant4-A Simulation Toolkit. *Nuclear Inst. and Methods in Physics Research, A*, 506(3):250–303, 2003.

[18] N. Metropolis and S. Ulam. The Monte Carlo Method. *Journal of the American Statistical Association*, 44(247):335–341, 1949.

[19] R. Brunn and F. Rademakers. ROOT-An Object Oriented Data Analysis Framework. *Paper presented at the AIHENP conference in Laussanne 1996*, 1996.

[20] Tsunefumi Mizuno et al. *Software for simulating PoGOLite with Geant4*. PoGOLite collaboration internal document.

[21] Olle Engdegård. Studies of Energy Dependent X-ray Polarisation with PoGOLite - Monte Carlo Simulations with Geant4. Master's thesis, KTH, 2006.

[22] T.W. Armstrong, B.L. Colborn, K.L. Dietz, and B.D. Ramsey. Neutron induced background in the mixe x-ray detector at balloon altitudes. *High Energy Radiation Background in Space, 1997 Conference on the*, pages 82–85, 1998.

[23] J.P. Wellisch and J. Apostolakis. Physics lists for use cases of Geant4 which involve hadronic processes. `http://geant4.web.cern.ch/geant4/physics_lists/` Accessed August 27, 2007.

[24] T. W. Armstrong, K. C. Chandler, and J. Barish. Calculations of neutron flux spectra induced in the earth's atmosphere by galactic cosmic rays. *Journal of geophysical research*, 78(16):2715–2726, June 1973.

[25] E. J. Zimmerman. Scintillation response of anthracene to low-energy protons and helium ions. *Physical Review*, 99:1199–1203, 1955.

[26] N. Nakao, T. Nakamura, M. Baba, Y. Uwamino, N. Nakanishi, H. Nakashima, and S.i. Tanaka. Measurements of response function of organic liquid scintillator for neutron energy range up to 135 mev. *Nuclear Instruments and Methods in Physics Research Section A Accelerators Spectrometers Detectors and Associated Equipment*, 362:454–465, 1995. doi:10.1016/0168-9002(95)00193-X.

[27] Tune Kamae. Private communication, April 2007.

[28] Tsunefumi Mizuno. *Proton/alpha background flux models*, October 2003. PoGOLite collaboration internal document.